THE ROLE OF HYPOXIA INDUCIBLE FACTOR 1 (HIF1)

IN THE RADIORESISTANCE OF MENINGIOMAS

by

Michael A. Karsy

A thesis submitted to the faculty of
The University of Utah
in partial fulfillment of the requirements for the degree of

Master of Science

Department of Bioengineering

The University of Utah

December 2017

The University of Utah Graduate School

STATEMENT OF THESIS APPROVAL

The thesis of **Michael A. Karsy**

has been approved by the following supervisory committee members:

Robert Hitchcock	, Chair	**6/14/17**
		Date Approved
Robert Bowles	, Member	**6/13/17**
		Date Approved
Randy L. Jensen	, Member	**5/31/17**
		Date Approved

and by **David W. Grainger** , Chair/Dean of the Department/College/School of **Bioengineering**

and by David B. Kieda, Dean of The Graduate School.

ABSTRACT

Meningiomas are the most common primary brain tumors, accounting for 36.6% of all tumors with ~20,000 cases annually in the U.S. Although 65–80% of cases are benign (World Health Organization [WHO] Grade I), recurrence over a long period can be seen, especially for subtotal resections and higher-grade tumors (II and III). Radiotherapy is a common primary or adjuvant therapy, but its mechanisms of action in the setting of distinct subtypes of meningioma remain unknown. Hypoxia-inducible factor 1 (HIF1) plays a key role in cellular response to oxygen tension, modulates multiple downstream genes, controls tissue vascularization, and may serve as a resistance-promoting mechanism in tumors. The aim of this study was to evaluate the clinical impact of the HIF1-signaling pathway in meningioma characterization as well as the impact of radiotherapy on meningiomas in the setting of HIF1 knockout. Clinical samples from patients with meningiomas, primary derived cell lines (GAR, JEN, SAM, MCT, BSH, IOMM-LEE), and HIF1 generated knockouts (GAR-1589) were utilized. Multiple immunohistochemical markers and a fractal-based microvascularity quantification showed that Grade I meningiomas ≥3 cm showed greater staining for MIB and von Willebrand Factor as well as an average 19-month shorter survival. In addition, a MIB index ≥3 showed high specificity (82.5%) but not sensitivity (36%) for predicting progression-free survival. Cell proliferation and apoptosis in response to radiation doses

depended on cell density, *HIF1A* mutational status, and oxygen tension. Higher plated densities of cells showed resistance to radiation for various primary meningioma cell lines. GAR cells demonstrated greater response to high-dose radiation than GAR-1589 cells in 2D and 3D cultures, while neither cell line responded to fractionated radiotherapy. Hypoxic environments reduced the efficacy of radiation, in fact showing increased cell proliferation with low doses of radiation. GAR-1589 cell, however, showed greater increases in cell apoptosis during radiotherapy in normoxic environments than GAR cells. Multimodal imaging using tumor bioluminescence, positron emission tomography tracers, and MRI showed potential for evaluating various characteristics of primary brain tumors noninvasively using an orthotopic rodent model. These results offer some correlation clinically and experimentally regarding the importance of HIF1 and tumor resistance.

TABLE OF CONTENTS

LIST OF TABLES

LIST OF FIGURES

LIST OF ABBREVIATIONS

AKT1: v-akt murine thymoma viral oncogene homolog 1

ANOVA: Analysis of variance

ARNT: Aryl hydrocarbon receptor nuclear translocator, HIF-1β

bHLH: Basic helix-loop-helix

CA-IX: carbonic anhydrase 9

CI: confidence interval

CRISPR: Clustered regularly interspaced short palindromic repeats

CSC: Cancer stem cell

C-TAD: C terminus domain

Cu-ATSM: ^{64}Cu-ATSM Cu-diacetyl-bis(N4-methylthiosemicarbazone)

DAL-1: Differentially expressed in adenocarcinoma of the lung

DMEM: Dulbecco's modified Eagle's medium

EBL: Estimated blood loss

EGFR: Epidermal growth factor receptor

ELISA: Enzyme-linked immunosorbent assay

ERBB2: Erb-B2 receptor tyrosine kinase 2

FACS: Fluorescence-activated cell sorting

FDG: ^{18}F-fludeoxyglucose

FET: O-(2-^{18}F-fluoroethyl)-L-tyrosine

FGF: Fibroblast growth factor

FH: Fumarate hydratase

FLT: ^{18}F-fluorothymidine

FMISO: ^{18}F-labeled fluoro-misonidazole

FRP-170: 1-(2-[(^{18})F]fluoro-1-[hydroxymethyl]ethoxy)methyl-2-nitroimidazole

GFP: Green fluorescent protein

GLUT-1: Glucose transporter 1

HIF-1: Hypoxia-inducible factor 1

HIF-1α: Hypoxia-inducible factor 1 subunit alpha

HIF-1β: Hypoxia-inducible factor 1 subunit beta, ARNT

HIF-2: Hypoxia-inducible factor 2

IDH1/2: Isocitrate dehydrogenase 1 and 2

IHC: Immunohistochemistry

KLF4: Kruppel-like factor 4

LB: Luria broth

MAPK: Mitogen-activated protein kinase

MCP-1: Monocyte chemoattractive protein-1

MN: Metronidazole

MRI: Magnetic resonance imaging

mTOR: Mechanistic target of rapamycin

NF2: Neurofibromin 2

N-TAD: N terminus domain

ODD: Oxygen-dependent degradation domain

OR: Odds ratio

OS: Overall survival

PAI-1: Plasminogen activator inhibitor-1

PET: Positron emission tomography

PFS: Progression-free survival

PI3K: Phosphoinositide-3-kinase

PIK3R1: Phosphatidylinositol 3-kinase regulatory subunit alpha

PHD: Prolyl hydroxylase domain-containing

PML: Promyelocytic leukemia

POLR2A: Catalytic subunit of RNA polymerase II

PRKAR1A: Protein kinase CAMP-dependent type I regulatory subunit alpha

PTEN: Phosphatase and tensin homolog

ROC: Receiver operating characteristic

SD: Standard deviation

SDH: Succinate dehydrogenase complex

SMO: Smoothened, frizzled family receptor

SUFU: SUFU negative regulator of hedgehog signaling

TIMP1, TIMP3: Tissue inhibitors of metalloproteinases 1 and 3

TNF: Tumor necrosis factor

TRAF7: TNF receptor-associated factor 7

TSC1/TSC2: Tuberous sclerosis 1/2

uPAR: Urokinase receptor

VEGF: Vascular endothelial growth factor

VHL: Von Hippel-Lindau

vWF: von Willebrand factor

WHO: World Health Organization

WNT6: Wnt family member 6

ZIC1/ZIC4: Zinc finger protein ZIC 1/4

ACKNOWLEDGMENTS

For my wife Odessa who has tirelessly supported me, believed in me, and cared for our children Penelope and Philip during the countless hours in lab or class. Thank you for encouraging me to take a chance. I am also grateful to my parents, Sheila and Allen, and brother, Meelad, who didn't think it was weird at all for me to go back to graduate school.

I'd like to thank Randy L. Jensen who supported me in his lab, was always open to new ideas, and served as a strong neurosurgeon-scientist mentor. To David L. Gillespie, I have learned a tremendous amount from you both in science and in perseverance. This work could not have been done without you. To my committee members, Robert Hitchcock and Robby Bowles, thank you for your guidance. Bob, I will remember my many talks with you about device design, engineering, and the wonderful system at the FDA. Dr. Bowles, thank you for offering some fresh perspective on our research.

To Nick Quinn, Meridith Wendland, Jonathan Harper, and other students in the lab, thank you for your help. Your work allowed the next step. Regarding Kevin Horn, Lance Burrell, and Jeffrey Yap, thank you for your support from the Center for Quantitative Cancer Imaging at the Huntsman Cancer Institute in imaging animals as well as discussing imaging methods. For Timothy J. Dahlem in the CRISPR core lab and

James Marvin in the Flow core lab at the University, I appreciate your help. With special mention to Kristin Kraus who has helped with editorial support on pretty much every project, always seeking to help residents publish their work, and with unending positive enthusiasm!

And lastly with thanks to our generous financial supporters, including the Huntsman Research Foundation, Meningioma Mommas, and Department of Neurosurgery.

Portions of this work have been previously published:

- Karsy M, Burnett B, Di Ieva A, Cusimano MD, Jensen RL. Microvascularization of Grade I meningiomas: effect on tumor volume, blood loss, and patient outcome. J Neurosurg. 2017 Mar 31:1-10.{Karsy, 2017 #1032}
- Karsy M, Guan J, Jensen R, Huang LE, Colman H. The impact of hypoxia and mesenchymal transition on glioblastoma pathogenesis and cancer stem cells regulation. World Neurosurg. 2016 Apr;88:222-36.{Karsy, 2016 #907}

Portions of this work have been submitted for publication:

- Karsy M, Gillespie DL, Jensen RL. The role of hypoxia-inducible factor 1-alpha is critical in the radioresistance of meningioma. *Submitted 2017*
- Karsy M, Gillespie DL, Horn KP, Burrell LD, Yap JY, Jensen RL. Correlation of Glioma Proliferation and Hypoxia by Luciferase, Magnetic Resonance, and Positron Emission Tomography Imaging. *Submitted, 2017.*
- Karsy M, Gillespie DL, Horn K, Guan J, Brock AA, Jensen RL. Magnetic Resonance Imaging (MRI) of Hypoxia in Primary Central Nervous System Tumors. Part 1. *Submitted*, 2017

- Karsy M, Gillespie DL, Horn K, Ruesch M, Harper J, Jensen RL. Positron Emission Tomography (PET) of Hypoxia in Primary Central Nervous System Tumors. Part 2. *Submitted*, 2017

CHAPTER 1

INTRODUCTION

1.1 Natural history of meningiomas

Coined by Harvey Cushing in 1922, meningiomas are primary central nervous system tumors arising in the brain and spine from the arachnoid cap cells of the meninges (1, 2). Meningiomas are divided into World Health Organization (WHO), Grades I through III, and with an average incidence of 8.03:100,000 people in the U.S. are the most common primary brain tumors, accounting for 36.6% of all tumors with approximately 26,000 new cases predicted in 2017 alone (3). Autopsy studies suggest that 20-30% of the population harbor meningiomas (4).

Meningiomas vary with recurrence depending on Simpson grade of resection. Approximately 65-80% of meningiomas are Grade I, with 95% 5-year progression free survival for Simpson Grade I resections and a local 5-year recurrence rate of 7-23% depending on grade of resection (5-7). According to the 2016 WHO criteria, Grade II (atypical) meningiomas are defined with a mitotic index ≥4 per 10 high-power fields, 3 of 5 parameters (sheeting architecture, small cell formation, macronucleoli, hypercellularity, spontaneous necrosis), brain invasion, choroid pathology, or clear cell pathology (2, 8). Grade III (anaplastic) meningiomas show mitotic index ≥20 per 10 high-power fields, anaplasia, papillary pathology or rhabdoid pathology. Grade II meningiomas account for

20-35% of meningiomas and show local control rates of 68-83% at 5 years while grade III meningiomas account for 3% of all meningiomas and show local control rates of 17-52% at 5 years (7).

Treatments for meningiomas beyond surgery include external beam radiation therapy, stereotactic radiosurgery, and chemotherapy. Only three systemic therapies, alpha-interferon, somatostatin receptor agonists, and vascular endothelial growth factor inhibitors, have been recommended by the National Comprehensive Cancer Network for treatment of recurrent meningioma (9). In fact, treatments evaluated *in vitro* and *in vivo* have failed to reach clinical due to difficulty in drugs passing the blood-brain barrier and models of meningioma (10). Limitations in expanding treatment options for patient with meningioma include the slow growth of meningiomas, and limited understanding of molecular underpinnings of the disease.

1.2 Current molecular understanding of meningiomas

Several tumor suppressor and oncogenes have been implicated in the pathogenesis of meningiomas [Reviewed by Pham et al. 2011 (11)]. *NF2,* (*Neurofibromin 2*), localized in chromosome 22q, is lost in approximately 60% of meningiomas and altering cytoskeletal structure. *DAL-1* (*differentially expressed in adenocarcinoma of the lung*) is also mutated in 60% of meningiomas and plays a role in actin binding and cytoskeletal structure. *TIMP1* and *TIMP3* (*Tissue inhibitors of metalloproteinases*) regulate matrix metalloproteinase activity and are implicated in cell proliferation, and infiltration of meningiomas. *CDKN2A* and *CDKN2B*, found on chromosome 9p, are mutated in 46% of anaplastic meningiomas and 3% of atypical meningiomas, impacting cell cycle regulation. Several key oncogenes, such as *c-sis*, *c-myc*, *c-mos*, and *c-fos*, have been

implicated in meningioma cell growth and tumorigenesis. Apoptosis regulating genes, *TP73* and *bcl-2*, are also often mutated in meningiomas.

Recent genomic expression studies of meningiomas have offered additional insight into key mutations and genomic subtypes. A study by Clark et al. utilizing a gene expression array of 300 meningiomas, identified *NF2*, *TRAF7* (*TNF receptor-associated factor 7*), *KLF4* (*Krupple-like factor 4*), *AKT1* (*v-akt murine thymoma viral oncogene homolog 1*), and *SMO* (*Smoothened, frizzled family receptor*) as commonly mutated genes (12). Interestingly, *NF2*, *KLF4*, *AKT1*, and *SMO* mutations were found localized to the posterior fossa, sphenoid wing, midline tuberculum sellae, and cribiform plate, respectively. A subsequent genomic study of 775 meningiomas identified mutations in *POLR2A* (*catalytic subunit of RNA polymerase II*) as a key oncogenic driver which regulates a number of downstream genes including, WNT6 (Wnt Family Member 6) and *ZIC1/ZIC4* (*Zinc finger protein ZIC 1*) (13). Other identified genes were *AKT3*, *PIK3R1* (*Phosphatidylinositol 3-kinase regulatory subunit alpha*), *PRKAR1A* (*Protein Kinase CAMP-Dependent Type I Regulatory Subunit Alpha*), and *SUFU* (*SUFU Negative Regulator Of Hedgehog Signaling*). These findings have shed new insight into the genomic subtypes of meningiomas with implications for targeted treatment and evaluating radioresponsiveness.

1.3 Impact of hypoxia and HIF1α on meningioma

Hypoxia, decreased normal oxygen tissue perfusion levels, is a common finding and pathogenic driver in a variety of primary brain tumors including meningioma and gliomas (14-17). Various reasons for hypoxia in tumors include increased cell proliferation rates, inefficient neovascularization, limited oxygen diffusion, alterations of

the blood-brain barrier, poor nitric oxide permeability, and formation of a hypoxic, necrotic microenvironment (18). Hypoxic areas in meningiomas, and upregulation of hypoxia inducible factors (HIFs) which are stabilized during hypoxia, correlate with more aggressive meningiomas (15, 19), development of both meningiomas and gliomas (20), regulation of the tumor microenvironment (14, 21), as well as correlation with both diffusion restriction from absent blood flow seen on MRI (22) and necrosis (23). Hypoxic conditions also upregulated downstream proteins from HIFs in meningioma, such as VEGF (24).

HIFs play a critical role in the hypoxic microenvironment of cancer cells including meningioma (25) (Figure 1.1). HIFs were initially discovered during the identification of a hypoxia response element in the 3' enhancer of erythropoietin (26, 27). HIF-1 and HIF-2 are involved in cell survival when transitioning from normoxia (21% O2) to hypoxia (1% O2). HIF-1 consists of the oxygen-sensitive HIF-1α and constitutively expressed HIF-1β (also known as aryl hydrocarbon receptor nuclear translocator [ARNT]) subunits (28). Each subunit contains a basic helix-loop-helix (bHLH), PAS, and C terminus (C-TAD) domain, while HIF-1α contains an additional oxygen-dependent degradation domain (ODD) and N terminus domain (N-TAD). The bHLH and PAS domains are involved in heterodimer formation and binding to hypoxia response element DNA sequence in the promoter of HIF target genes, whereas the N-TAD and C-TAD domains are involved in transactivation through interactions with the transcriptional coactivators p300/CBP (29-31). The ODD domain is specific to HIF-1α and is involved in mediating oxygen-regulated stability (32). Hypoxia inhibits prolyl hydroxylation, resulting in HIF-1α stabilization, nuclear translocation, dimerization with HIF-1β, and gene transactivation (26, 33, 34). The well-characterized HIF-α isoforms

include HIF-1α and HIF-2α, with HIF-1α seen in essentially all cell types and HIF-2α common in endothelial cells and cancer stem cells (CSCs) (35, 36). In normoxia, HIF-1α (Pro-402, Pro-564) and HIF-2α (Pro-405, Pro-531) are subjected to prolyl hydroxylation by a family of prolyl hydroxylase domain-containing (PHD) proteins, which induces binding of the tumor suppressor von Hippel-Lindau (VHL) for polyubiquitination and 26S proteasomal degradation (30, 37). Factor-inhibiting HIF-1 (FIH1) is also a hydroxylase that blocks p300 interaction with HIF-1α through Asn803 modification (38). Multiple oncogenes and tumor suppressors also modulate HIF regulation at a protein and DNA level (39).

Approximately 100 genes regulated by HIFs and hypoxia are involved in angiogenesis, senescence, migration, cell survival, and proliferation, but the complete understanding regarding the alterations of specific genes and their clinical significance in primary brain tumors remain to be better explored (40-42). In addition, multiple signaling pathways upstream of HIF-1 regulate its expression and are altered in a variety of tumors. Mutation of tumor suppressors such as LKB1, promyelocytic leukemia (PML), phosphatase and tensin homolog (PTEN), and tuberous sclerosis 1/2 (TSC1/TSC2) can result in mechanistic target of rapamycin (mTOR) dysregulation and subsequent upregulation of HIF-1α(43). Similarly, up-regulation of upstream genes, such as the protein tyrosine kinases Erb-B2 receptor tyrosine kinase 2 (ERBB2) and epidermal growth factor receptor (EGFR), as well as Ras or phosphoinositide-3-kinase (PI3K), can induce HIF-1α through mTOR dysregulation. Mutation of tumor suppressor p53 (p53) may also increase HIF activity by disrupting MDM2-mediated degradation of HIF-1α(44). A variety of critical oncogenic pathways downstream from HIF-1α serve as key regulators of tumor progression and resistance. Various tumor suppressors (e.g., Von

Hippel-Lindau tumor suppressor [VHL], succinate dehydrogenase complex [SDH], fumarate hydratase [FH], isocitrate dehydrogenase 1 and 2 [IDH1/2], p53, TSC2, PTEN, and LKB1), oncogenic signaling pathways (e.g., mitogen-activated protein kinase [MAPK], PI3K/AKT), and inflammatory pathways (e.g., tumor necrosis factor [TNF], IL-1, IL-5, IL-8) show significant cross-talk with HIF-1α (45).

1.4 Role of microvascularity in meningiomas

Microvascularity and abnormal vessel growth in tumors as a response to hypoxia also plays various oncological roles. The quantitative assessment of tumor microvascularity and its impact on aggressiveness was first explored by Folkman and others in the 1970s (46). Since then, multiple studies have shown the importance of hypoxia and microvascularity in tumor aggressiveness (25), prediction of patient survival (16), response to anti-angiogenic treatments (47, 48), regulation of cancer stem cells (49), and multiple oncological signaling pathways (50). Previous studies have shown the importance of *in vitro* vascular density in predicting meningioma recurrence (51, 52), as well as vascular endothelial growth factor (VEGF) expression and WHO grade (53, 54). Further elucidation of the underlying microvascular changes in meningioma may be an avenue for understanding tumor biology and designing future treatments.

Multiple methods of quantifying microvascularity in meningiomas and other tumors have been suggested. Each method for evaluating antibody stains of microvessels, such as CD31, CD34, CD105, and von Willebrand Factor (vWF), shows specific sensitivity and specificity (55-57). The most common method involves manual evaluation of microvascularity by quantifying the number of vessels per square millimeter in a hotspot or random region (50). Manual counting and automated quantitation of vessels on

histopathological slides have both been reported (55, 58). Di Ieva et al. (59) described a fractal-based algorithm to quantify microvascularity by using CD34-stained histopathological slides. This method has been used to differentiate tumor histopathological grade as well as to achieve "microvascular fingerprinting" of distinct tumors (60). Our previous work also demonstrated the correlation of meningioma grade and immunostains for angiogenic signaling pathway proteins, including VEGF and HIF-1 (15). These findings suggest that tumor vasculature plays a central role in the growth and invasion of meningiomas. Although tumor vascularity has been evaluated by various methods in a multiplicity of tumors, its comprehensive assessment by a single method in meningioma remains limited. In addition, the roles of microvascularity in surgical outcomes and role of automated quantification methods have not yet ben explored in meningiomas.

1.5 Imaging of hypoxia in primary brain tumors

A variety of novel PET and MR imaging techniques have recently been developed to better understand primary brain tumor pathophysiology in a noninvasive manner (16, 61, 62). PET tracers have been developed for assessment of angiogenesis, proliferation, and apoptosis *in vivo* (61). Moreover, hypoxia evaluation has been developed using a variety of tracers, including 2-nitroimidazole compounds [^{18}F-labelled fluoro-misonidazole (FMISO) or 1-(2-[(^{18})F]fluoro-1-[hydroxymethyl]ethoxy)methyl-2-nitroimidazole (FRP-170)], ^{64}Cu-diacetyl-bis(N4-methylthiosemicarbazone) (Cu-ATSM) or ^{99}mTc- and ^{68}Ga-labelled metronidazole (MN) agents (62). In addition, MR-specific modalities, such as MR perfusion and arterial spin labeling, can be useful in evaluating tumor vasculogenesis with implications for predicting tumor aggressiveness and type

(63). These tools can aid in identifying unknown lesions as potential tumors, delineating tumor grade and histology, predicting prognosis, identifying tumor for resection or biopsy, and predicting response to radiation.

Multimodal imaging can be useful in better understanding the impact of hypoxia in primary brain tumors. While these techniques may be relevant in meningiomas, they have been better studied in gliomas. FMISO is one of the most commonly explored agents in hypoxia imaging. FMISO is a ^{18}F-labeled, 2-nitroimidazole based compound which is reduced and retained in hypoxic cellular areas, binds covalently to cellular thiol macromolecules via an imidazole ring formed during reduction, and conjugates to intracellular glutathione (64-66). FMISO can be useful in predicting brain tumor diagnosis and grade, specifically with gliomas (67-69). In addition, combination with markers of cell proliferation, such as ^{18}F-fludeoxyglucose (FDG), ^{18}F-fluorothymidine (FLT) or O-(2-^{18}F-fluoroethyl)-L-tyrosine (FET), have been useful in evaluating primary brain tumors (70, 71). Combinations of proliferation and/or hypoxia tracers with bioluminescence labeled cells have been useful in exploring tumor pathogenesis (70-72). Although several primary glioma models exist, the evaluation of cell mutation, imaging performance, and treatment options can be more rapidly assessed via a syngenic orthotopic glioma model (73-75). Bioluminescence imaging with luciferase-capturing cameras can be used to evaluate luciferase-containing gene expression plasmids that have been transfected into gliomas (76-78).

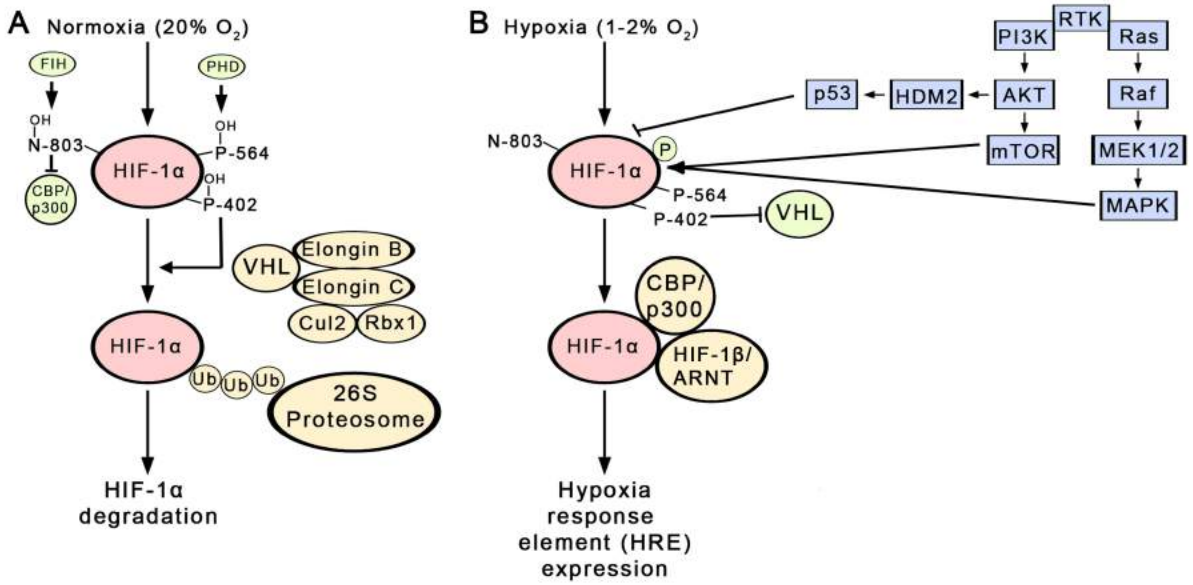

FIGURE 1.1: Regulation of hypoxia signaling

HIF signaling during normoxia and hypoxia as well as the interaction between HIFs and EMT are represented. A) During normoxia, increased activity of PHDs levels results in hydroxylation of HIF-1α residues (P-564, P-402), which recruits the VHL complex. Upregulation of FIH induces hydroxylation of HIF-1α residues (N-803) that suppressed CBP/p300 complex formation. Poly-ubiquitination of HIF-1α occurs by the VHL complex resulting in further recruitment of the 26S proteasomal complex and HIF-1α degradation. B) During hypoxia (1-2% O2), HIF-1α remains unhydroxylated, resulting in recruitment of HIF-1β/ARNT and the coactivator CBP/p300, which bind to hypoxia response elements involving expression of several hundred downstream transcription factors, including those involved in mesenchymal transformation. HIF-1α can be also upregulated by various downstream regulators from receptor tyrosine kinases (e.g., PI3K/AKT/mTOR, Ras/Raf/MAPK). ARNT: aryl hydrocarbon receptor nuclear translocator; CSC: cancer stem cell; Cul2: cullin 2; FIH-1: factor inhibiting hypoxia-inducible factor; HIF-1α: hypoxia-inducible factor 1α; HRE: hypoxia response element; MAPK: mitogen-activated protein kinase; MEK1/2: MAPK kinase; mTOR: mammalian target of rapamycin; PI3K: phosphatidylinositol-4,5-bisphosphate 3-kinase; PHD: prolyl hydroxylase domain-containing protein; Rbx1: ring-box 1, E3 ubiquitin protein ligase; VHL: Von-Hippel Lindau

Reprinted with permission from: Karsy M, Guan J, Jensen R, Huang LE, & Colman H (2016) The Impact of Hypoxia and Mesenchymal Transition on Glioblastoma Pathogenesis and Cancer Stem Cells Regulation. World Neurosurg 88:222-236. (25)

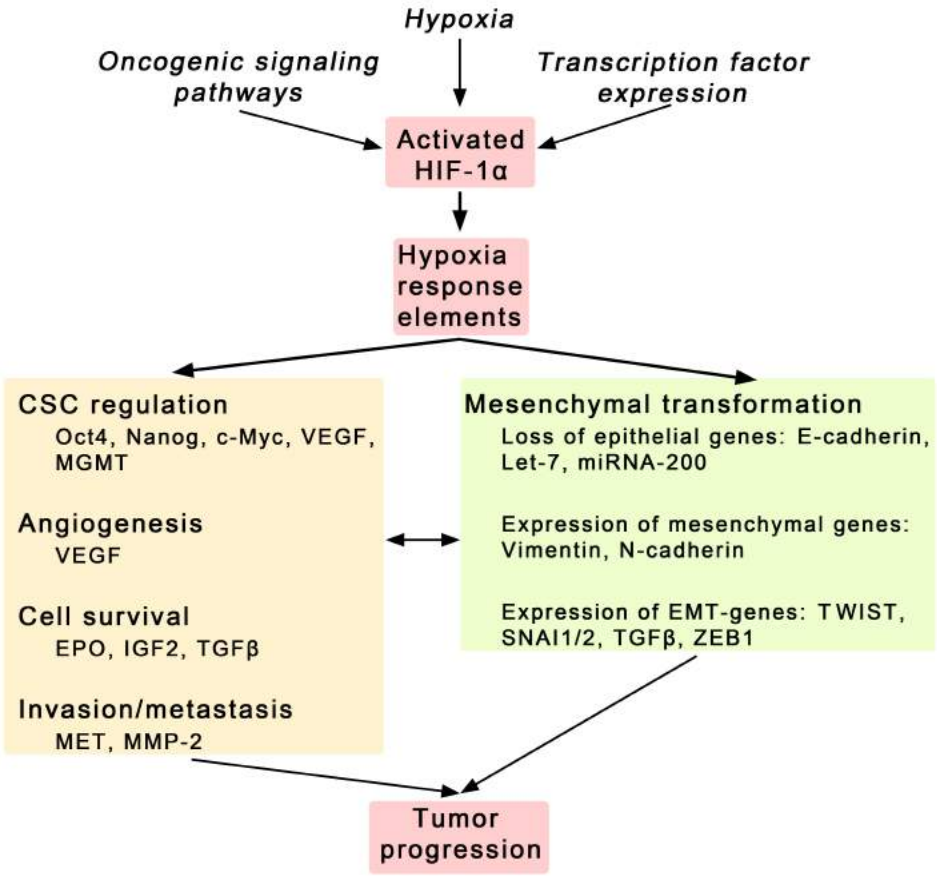

FIGURE 1.2: Downstream effects of regulating hypoxia signaling and mesenchymal transformation.

HIF-1α activation from hypoxia and oncogenic signaling pathways results in expression of various HIF-1 target genes via binding to hypoxia response elements. Multiple signaling molecules are involved in the regulation of CSCs, angiogenesis, cell survival, invasion/metastasis, and mesenchymal transformation. Upregulation of hypoxia signaling has been more clearly demonstrated in inducing mesenchymal transformation than the converse; however, hypoxia and mesenchymal transformation share many similar downstream activated regulators. Features suggestive of mesenchymal transformation include loss of epithelial genes, as well as expression of mesenchymal and EMT-regulating genes. CSC: cancer stem cell; EPO: erythropoietin; HIF-1α: hypoxia-inducible factor 1α; IGF2: insulin-like growth factor 2; miRNA: microRNA; MMP-2: matrix metallopeptidase 2; SNAI1/2: snail family zinc finger 1; TGFβ: transforming growth factor beta 1; TWIST: twist family BHLH transcription factor 1; VEGF: vascular endothelial growth factor; ZEB1: zinc finger e-box binding homeobox 1

Reprinted with permission from: Karsy M, Guan J, Jensen R, Huang LE, & Colman H (2016) The Impact of Hypoxia and Mesenchymal Transition on Glioblastoma Pathogenesis and Cancer Stem Cells Regulation. World Neurosurg 88:222-236. (25)

CHAPTER 2

MATERIALS AND METHODS

2.1 Cell lines

After receiving Institutional Review Board approval, acquired surgical samples were graded according to the 2007 World Health Organization guidelines and cultured cell lines were developed as previously described (79). Primary surgical specimen derived cell lines (GAR, JEN, SAM, MCT, BSH) were generated by the Jensen lab while IOMM-LEE was generously gifted from Dr. Ian McCutcheon (University of Texas, MD Anderson Cancer Center, Houston, TX) (80). GAR cells were developed from a 71-year-old male patient with a tentorial WHO I meningioma, JEN lines from a 55-year-old male with convexity WHO I meningioma, SAM cell lines from a 38-year-old female with olfactory groove, psammomatous WHO I meningioma, and IOMM-LEE cells from a 61-year-old male with WHO III interosseous meningioma. primary meningioma GAR cell lines were utilized for *in vitro* analysis of meningioma radiation response.

GAR1589 HIF1A knockout cells were generated using a hygromycin-inducible shRNA plasmid (Ambion; Thermo-Fisher) (Figure 2.1A). An shRNA targeting vector used to induce mRNA suppression at the 1589 nucleotide position of *HIF1A* was designed and inserted into a pSilencer 2.1 vector with U6 promoter and SV40-induced hygromycin resistance gene. Generated vector was verified by DNA sequencing of the

included U6 using forward primers (GGGCAGGAAGAGGGCCTAT). After routine bacterial amplification described below, purified plasmid was transfected using Lipofectamine 2000 (Thermo-Fisher, Waltham, MA), and single cell colonies were expanded. HIF1A activity was verified by Western blot and ELISA screening (Figure 2.1B,C).

F98 glioma cells were used for validation of *in vivo* animal models. A pMMP plasmid construct with upstream U3 and U5 promoters to a luciferase reporter (addgene.com) (Figure 2.1D). Cells were transfected by Lipofectamine 2000, and single cell colonies were expanded. Confirmed luciferase expression was identified upon culture with luciferin (Thermo-Fisher) and detected on an EnVision 2104 multilabel reader (PerkinsElmer, Waltham, MA).

Clustered regularly interspaced short palindromic repeats (CRISPR)/Cas9-mediated knockout of *HIF1A* in GAR cells was performed. A lentiviral CRISPR/Cas9 construct was created for *HIF1A* via the CRISPR core at the University of Utah (Figure 2.1E). The lentiviral system depended on 3 plasmids transfected in human kidney 293T cell lines followed by viral production. During Lipofectamine 2000-mediated transfection of 75cm^2 size flasks, 1170 µl of OptiMEM media (Thermo Fisher Scientific) was mixed with 3.9ug of VSVg, PSPAX and the CRSPER/Cas9 construct each as well as 1170 µl of OptiMEM media with 23.4 µl of Lipofectamine 2000 reagent. After combining the two media dropwise and incubation for at least 5 minutes, 293T cell transfection was performed and verified at 48 hours by green fluorescence protein (GFP) expression. After precipitation of cell debris at 8,000 rpm for 5 minutes and decanting clean supernatant, viral particles were purified by ultracentrifugation at 24,000g for 2 hours at 37^{o}C. Transfection of GAR cells plated overnight to reach 50% confluence was performed

followed by verification of CRISPR transfection by GFP expression (Figure 2.1F). Single cell sorting by BD 5-laser fluorescence activated cell sorting (FACS) Aria flow-cytometry (BD Biosciences, San Jose, CA) was performed (Figure 2.1G) and HIF1A knockdown was verified by ELISA.

Cells in monolayer were grown in Dulbecco's modified Eagle's medium (DMEM) (Sigma, St. Louis, MO) supplemented with 10% fetal bovine serum, L-glutamine (2 μmol/L), penicillin (50 IU/mL), and streptomycin (50 mg/mL). Cells were grown at 37°C in 5% CO2.

2.2 Human samples and imaging analysis

Patient demographic data and tumor tissue were collected from 1996 to 2011 in an Institutional Review Board–approved prospective surgical database of patients with diagnosed cerebral meningiomas operated on by the senior author (RLJ). Cases were diagnosed based on the 2007 WHO guidelines with adjustment of cases diagnosed prior to 2007 based on new criteria when applicable. Analysis was limited to patients with grade I meningiomas (n=207 patients) who encompassed the majority of cases. Patient characteristics were retrospectively analyzed from surgical, anesthesia, and electronic medical records for patient outcome and estimated blood loss (EBL). Pathological specimens underwent standard formalin fixation and paraffin embedding followed by histopathological as well as immunohistological analysis. PFS was calculated from the date of diagnosis until the date of radiographic disease progression or last follow-up date. OS was calculated from diagnosis date until date of death or last follow-up.

Two methods of clinical tumor volume measurement were used. First, volume was calculated by using T1-weighted magnetic resonance imaging (MRI) with contrast to

determine maximal length (cm) × width (cm) × depth (cm) × 0.5. Second, volumetric measurements of regions of interest were summed on each imaging slice using OSIRX software (Version 7.5, http://www.osirix-viewer.com/).

2.3 Plasmid amplification

Plasmid amplification was performed in *E. Coli* by routine methods. Plasmid (1µl, 100-300ng/µl) was transfected in 40µl of STbl3 competent *E. Coli* cells with using a heat shock method. Cells were mixed with plasmid, kept on ice for 30 minutes, subjected to heat shock at 42^{o}C for 45 seconds followed by incubation on ice for 5 minutes before plating on Ampicillin containing luria broth agar plates. After overnight incubation at 37^{o}C, single colonies were subcultured in 5ml of Ampicillin-containing LB media for 2 hours prior to culturing. Frozen stocks of single cultures were in 50% glycerol containing stocks, followed by flash freezing in liquid nitrogen, and storage at -80^{o}C. Expanded culture was used for DNA extraction by Miniprep or Maxiprep (Qiagen, Hilden, Germany) and plasmids were verified by Sanger DNA sequencing using the University DNA sequencing core lab.

2.4 Hypoxia chamber

For hypoxia cultures and treatment, cells were incubated at 37°C in 5% CO2 and 1% oxygen saturation with use of nitrogen gas as a buffer in a ProOx model C21 hypoxia chamber (Biospherix, Lacona, NY). Cell irradiation under hypoxic conditions involved sealing cell plates during treatment.

2.5 Cell viability

After cell seeding on 96-well opaque plate (4000 cells/well), and allowing overnight adhere, cells were treated with doses of radiation over 1–3 days. The CellTiter-Glo assay (Promega, Madison, WI) was used for chemiluminescent detection of cell viability. Cells were detected on an EnVision 2104 multilabel reader (PerkinsElmer, Waltham, MA). This assay offered better sensitivity than other methods.

For MTT (Sigma) assay, cells were plated on a 96-well clear bottom plate (4000 cells/well), allowed to adhere overnight, and underwent appropriate treatments. Cell media was replaced with phosphate-buffered saline, and MTT reagent was incubated for 2 hours at 37°C. Formazan crystals were dissolved in dimethyl sulfoxide and read at 495 and 530 nm on a Benchmark Microplate Reader (Biorad).

For evaluation of live cell proliferation and confluency, cells were seeded on 6-, 12- or 24-well plates at 50% starting confluency. Cells were allowed to adhere to the plate for 24 hours followed by single radiation treatment (10 or 20Gy). Hourly images were taken in 4-9 quadrants via the IncuCyte Zoom (Ann Arbor, MI) at 10X. Image confluency was assessed by automated cell counting after image training. Counted fields were averaged to make a final hourly measurement.

2.6 Cell counts

Cells were plated at a known concentration (1.3 × 107) on 60-mm culture dishes and passaged daily with replacement of media. For cell counting, cells were harvested with trypsin, 10 µl of cells and 10 µl of Trypan Blue (Sigma) were mixed, and 10 µl of this was placed on counting cuvettes and evaluated by Countess II Automated Cell Counter (Thermo Fisher Scientific). Cell doubling times were calculated by

approximating an exponential growth curve doubling time = duration × log(2)/log(final) – log (initial).

Dilutional cell assays involved plating 10–10000 cells per well in a 96-well plate, which represented a range of <1% to 25% in cell confluency. Cell confluency was evaluated up to 6 days with or without treatment, and MTT assay (below) was also performed.

2.7 Radiation treatments

Radiation dosages of 2–20 Gy were delivered at a rate of 1449 cGy/min to cultured cell via a RS-2000 (Rad Source, Suwanee, GA). Cells in 96-well plates were placed in a custom-built lead-shielded device to selectively irradiate wells (Figure 2.2A,B). The evaluations of radiation dosages and the adequacy of shielding to limit dosages were performed weekly.

2.8 Apoptosis Evaluation

Cell apoptosis was evaluated using the ApoLive-Glo Multiplex Assay (Promega). Cells were seeded on a 96-well opaque plate (4000 cells/well), underwent treatment, and were analyzed according to manufacturer instructions for viability by fluorescence and caspase 3 activities by luminescence on an Envision 2104 multilabel reader (PerkinsElmer).

2.9 Colony Formation Assay

After formation of a base layer of 1:1 mixture of 1% agar and DMEM, cells ($5x10^4$) mixed with 1% agar at 37^oC and layered on the base in 6-well plates. After agar

hardening and overnight incubation, cells underwent respective radiation treatments. Cells were then incubated for 3 weeks with placement of new media every 2-3 days to avoid agar dessication. Cell colonies were stained with 0.5ml of 0.005% crystal violet in phosphate buffered saline and gentle rocking for 1 hour. Colony counting was performed prior to staining with dark field microscopy using the EVOS FL Cell Imaging System (Thermo Fisher) and after staining using a Leica MD641 microscope with DFC7000T camera (Leica, Wetzlar, Germany). Particle analysis was performed with ImageJ (https://imagej.nih.gov/ij/) using a minimum particle size of 20 pixel2.

2.10 Western blots

Western blots were performed by running 25 μg of protein on a 4–12% bis-Tris polyacrylamide gel (Novex/Thermo Fisher Scientific, Waltham, MA) after denaturation in 10% sodium lauryl sulfate dye (Thermo Fisher Scientific) at 65°C for 10 minutes. After blocking with 5% nonfat milk in tris buffered saline with 1% w/v tween overnight at 4^{o} C. Primary HIF1A (1:200, Santa Cruz, Santa Cruz, CA) and secondary mouse IgG-horseradish peroxidase conjugated (1:2500, GE Healthcare, Little Chalfont, UK) antibody detection was performed followed by detection using SuperSignal (Thermo Fisher Scientific) and autoradiography film (Hyblot, Metuchen, NJ).

2.11 Enzyme-linked immunosorbent assay (ELISA)

ELISA analysis of HIF1α is performed using a standard kit (Thermo Fisher Scientific). Fifty μl aliquots of samples are deposited in a 96-well well with coated primary antibodies for HIF1α. Secondary complementary IgG antibodies are added along with developing solution resulting in colorimetric reaction which is quantified by a

Biorad Benchmark Microplate Reader (Biorad, Hercules, CA) at 550 nm and 450 nm absorbance. Standard HIF1α protein is used as a control to correlate absorbance to protein level. All samples were performed in duplicate.

2.12 Immunohistochemistry (IHC)

IHC of of paraffin-embedded tissue blocks from rodents or clinical samples was performed for MIB-1 proliferation index, microvascularity and hypoxia-regulated proteins as previously described as previously described (81). The slides for MIB-1 were stained using Ki-67 antibody (Dako, clone MIB-1, dilution 1:300). The slides for the microvascularity analysis were pretreated with Factor VIII/vWF (rabbit polyclonal, dilution 1:100), PECAM-1/CD31, (Dako, clone JC70A, dilution, 1:100 for 1 hour at 37^{o}C. or endoglian/CD105 (Abcam, rabbit polyclonal, dilution was 1:100 for 1 hour at 35^{o}C) HIF-1α immunohistochemistry was performed using the Catalyzed Signal Amplification System (DAKO, Carpinteria, CA) with primary antibody, H1α67 (Novus Biologicals, Littleton, CO), at a dilution of 1:1000. VEGF, CA-IX, and glucose transporter 1 (GLUT-1) immunohistochemistry was done using anti-VEGF Ab-1 polyclonal antibody (1:50 dilution; Calbiochem, Cambridge, MA), anti-CA-IX goat polyclonal antibody (1:200; Santa Cruz Biotechnology, Santa Cruz, CA), or rabbit anti-GLUT-1 (1:100, Santa Cruz Biotechnology). Positive controls for MIB-1 were performed on human thymus, which has >90% cell staining. Positive controls for HIF-1α, VEGF, CA-IX, and GLUT-1 were performed on paraffin-fixed sections of tumors grown in mice using human U251 cell lines that were known to be immunohistochemically positive. Negative controls replaced the primary antibody with nonimmune serum.

All slides were examined under 200× magnification using an Olympus BX41

microscope and scored by an two investigators blinded to the patient information and tumor grade. The immunohistochemical analysis of HIF-1α, VEGF, CA-IX, and GLUT-1 was scored from 0 to 4 (0: 0%–<25%; 1: 25%–<50%; 2: 50%–<75%; 3: 75%–<100%; and 4: 100%) based on the number of cells stained in a given field.

The microvascularity index was calculated based on a previously published method (82). Briefly, three pictures of the most vascular area of the slide were taken at 400× magnification using an Olympus Microfire camera using Image-Pro Plus 5.0 and transferred to Photoshop CS 7 (Adobe Systems Incorporated, San Jose, CA). Any positive cell that was separate from other stained cells and not contiguous or branching from other vessels was counted. The results for each slide were averaged for the resulting microvascularity and divided by 0.26 mm2 to normalize the size of the picture field. The ratio of CD31, vWF, or CD105 positive to negative cells in 3 high power (100x) fields was calculated and averaged.

MIB-1 proliferation index was calculated using Ki-67 (clone MIB-1, dilution 1:300) as previously described (81). PI was calculated as the number of MIB-1-stained cells divided by the total number of cells in the field repeated 3 times for each picture and averaged. Two observers duplicated analysis. This method was reproducible, as demonstrated by good inter-rater (ρ=0.99, 95% CI [0.99–1.00]) and intra-rater (ρ=0.96, 95% CI [0.92–0.99]) reliability in prior studies (81).

2.13 Fractal-based microvascular assessment

Methods of fractal-based analysis of vascular density were used as previously described by Di leva et al. (59). Briefly, the microvascular patterns of CD34 immunostained histological slides were assessed by means of a parameter based on the

fractal dimension, that is the space-filing property of an irregular object by a regularly repeating geometric pattern at every scale (Figure 2.3). The local box-counting dimension (Loc bcD) was computed on each slide. Loc bcD is calculated in the "hot-spot" area of the histological slide by identifying the minimum number of differently sized boxes needed to cover an object in a defined range of magnifications (defined "scaling window"). The hot-spot area was defined as the 1 mm^2 most vascularized area of the slide (automatically selected by the software). The microvascular ratio, defined as the ratio between the immunopositive vessels over the tumor area, served to define the hot-spot.

2.14 Stereotactic intracranial injection

Rats were anesthesized with isoflurane prior to stereotactic orthotopic injection of primary tumor cells (method described in Karsy, Gillespie, Horn, Burrell, Yap, Jensen *submitted* 2017). Luciferase transfected F98 cells were used for validation of the *in vivo* model. Cells were prepared as described above, with $1.5x10^5$ cells/10µl mixed 1:1 with Matrigel (Corning, Corning, NY). Fisher rats (~100gm and 15 weeks old, Charles River, Boston, MA) were selected for injection (Figure 2.4). Animals were anesthetized via an incubation chamber then placed in a stereotactic head frame, fur was clipped, the skin cleaned with 70% ethanol, anesthetized with 1% lidocaine, and a linear midline incision was made from the midpuipillary to mid ocular point. After soft tissue dissection, the meeting of the coronal and sagittal sutures (e.g., bregma) was identified and a point 2mm posterior and 2mm lateral to the right was selected. A microdrill (ideal, Braintree Scientific, Braintree, MA) was used to penetrate the bone. A Hamilton 10µl syringe was used to inject 8µl of cells at a depth of 3mm from the skull over 1 minute. After removal

of the syringe, the burr hole was filled with bone wax and the skin was closed with 4-0 silk suture in an interrupted pattern.

2.15 Animal imaging

Animal bioluminescence was imaged using an IVIS Spectrum In Vivo Imaging System (PerkinElmer, Waltham, MA). Animals were anesthasized with isoflurane via an induction chamber. After subcutaneous or intraperitoneal injection of 0.5ml of 30mg/ml luciferin, and incubation for 5 minutes, animals were imaged for 10 minutes, using a focal length of 2.5cm. Averaged flux (lux/sec*cm) counts were obtained.

MR and PET imaging were performed in collaboration with Lance Burnell, Dr. Kevin P. Horn, and Dr. Jeffery T. Yap at the Center for Quantitative Cancer Imaging [CQCI]–Huntsman Cancer Institute. FMISO imaging of hypoxia and FLT imaging of proliferation were performed. These imaging methods have been recently described (Karsy, Gillespie, Horn, Burrell, Yap, and Jensen, *submitted 2017*).

2.16 Statistics

The means ± standard deviations (SDs) for all variables were calculated. Statistical analysis of continuous and discrete values was by T-test and Chi-squared test, respectively. Multiple means were compared by Analysis-of-variance (ANOVA) with Tukey post-hoc evaluation. Univariate linear analysis using Spearman's ρ was calculated, and variables with $p<0.25$ were entered into a multivariate, enter-method, linear regression. Correlation of various parameters was performed by bivariate linear correlation with reported correlation (r) and significance (p) values. Kaplan-Meier survival analysis with Mantel-Cox log-rank statistic was performed as well as a Cox

proportional hazards model with forward stepwise regression using likelihood ratio. A decision-tree analysis was performed for PFS and OS using Chi-squared automatic interaction detection method with maximum tree depth of 3 levels. Receiver operating characteristic (ROC) curves were used when identifying discrete values for microvascularity measurements. Statistical significance was defined as $p<0.05$, and statistics were calculated using SPSS (V20.0, Armonk, NY).

FIGURE 2.1: Plasmid maps and confirmation of transfected GAR meningioma cells

A) A shRNA construct targeting codon 1589 for HIF1α is shown. Hygromycin selection in eukaryotic cells can be performed. B) Confirmed downregulation of HIF1α is seen in GAR1589 cells for all treatment conditions, including normoxia (21% O_2), hypoxia (1% O_2) and after radiation treatments (4Gy radiation x 1 fraction). No difference in overall HIF1 expression is seen for GAR cells after treatments. However phosphorylation sites on GAR as well as downstream molecules to HIF1α could be involved during radiation exposure. C) HIF1α downregulation was confirmed by ELISA in GAR-1589 cells. D) A designed MMP-luciferase construct is shown for bioluminescence imaging of tumor cells. E) A designed lentivirus-CRISRP/Cas9 construct with gRNA for *HIF1A* with GFP selection. The construct requires cotransfection with separate VSVg and PSPAX plasmids for viral production. F) Selection of virus transfected cells with GFP expression is shown. G) FACS sorting of GFP expressing cells is shown (bottom) compared to control (top).

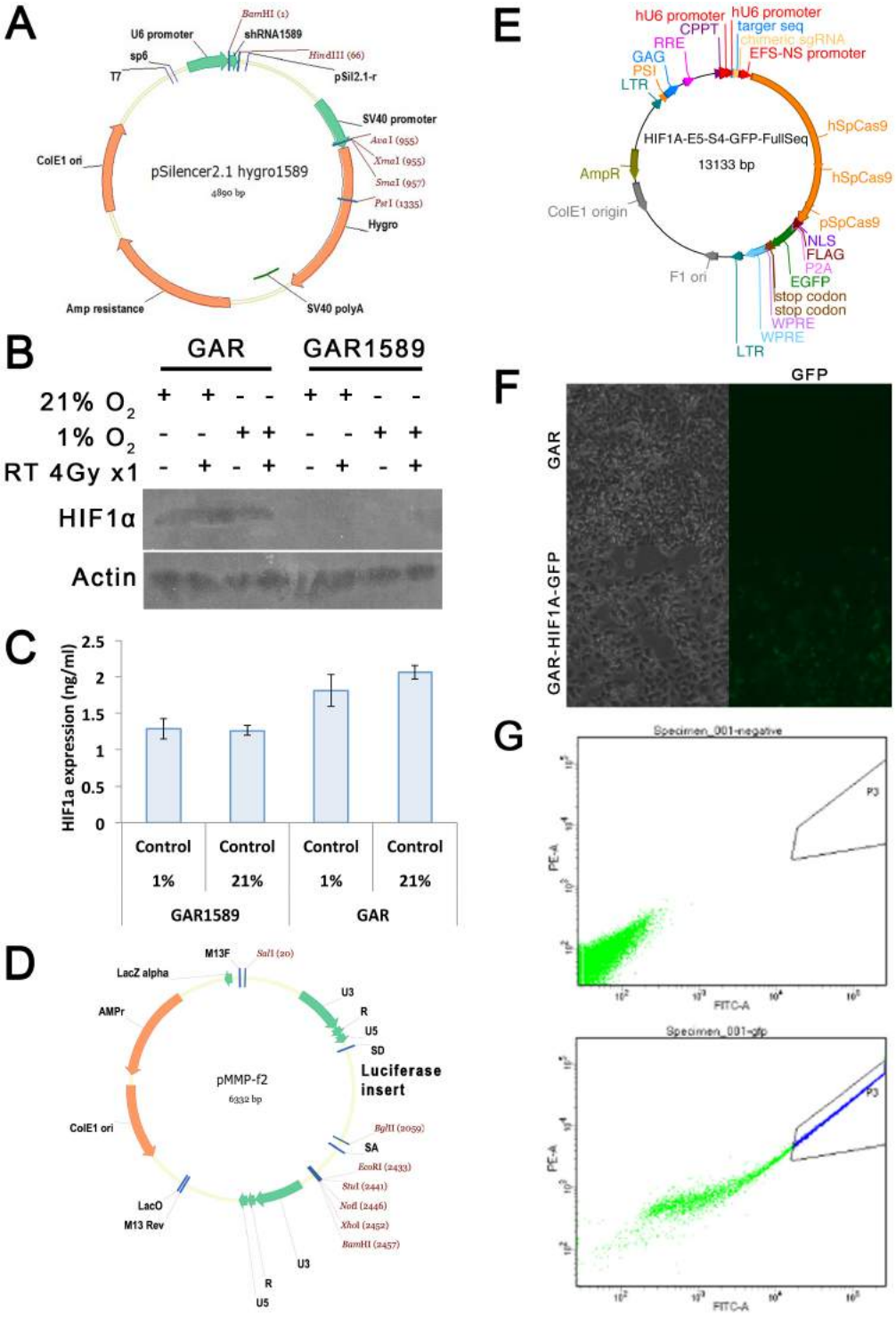
A
BamHI (1)
U6 promoter
shRNA1589
sp6
HindIII (66)
T7
pSil2.1-r
SV40 promoter
AvaI (955)
XmaI (955)
SmaI (957)
PstI (1335)
ColE1 ori
pSilencer2.1 hygro1589
4890 bp
Hygro
Amp resistance
SV40 polyA
B
GAR
GAR1589
21% O2 + + - - + + - -
1% O2 - - + + - - + +
RT 4Gy x1 - + - + - + - +
HIF1α
Actin
C
HIF1a expression (ng/ml)
2.5
2
1.5
1
0.5
0
Control 1%
Control 21%
Control 1%
Control 21%
GAR1589
GAR
D
M13F
SalI (20)
LacZ alpha
U3
AMPr
R
U5
SD
Luciferase insert
pMMP-f2
6332 bp
ColE1 ori
BglII (2059)
SA
EcoRI (2433)
StuI (2441)
NotI (2446)
XhoI (2452)
BamHI (2457)
LacO
M13 Rev
U3
R
U5
E
hU6 promoter
CPPT
hU6 promoter
targer seq
chimeric sgRNA
RRE
EFS-NS promoter
GAG
PSI
LTR
HIF1A-E5-S4-GFP-FullSeq
13133 bp
hSpCas9
AmpR
hSpCas9
ColE1 origin
pSpCas9
NLS
FLAG
P2A
F1 ori
EGFP
stop codon
stop codon
WPRE
WPRE
LTR
F
GFP
GAR
GAR-HIF1A-GFP
G
Specimen_001-negative
P3
PE-A
FITC-A
Specimen_001-gfp
P3
PE-A
FITC-A

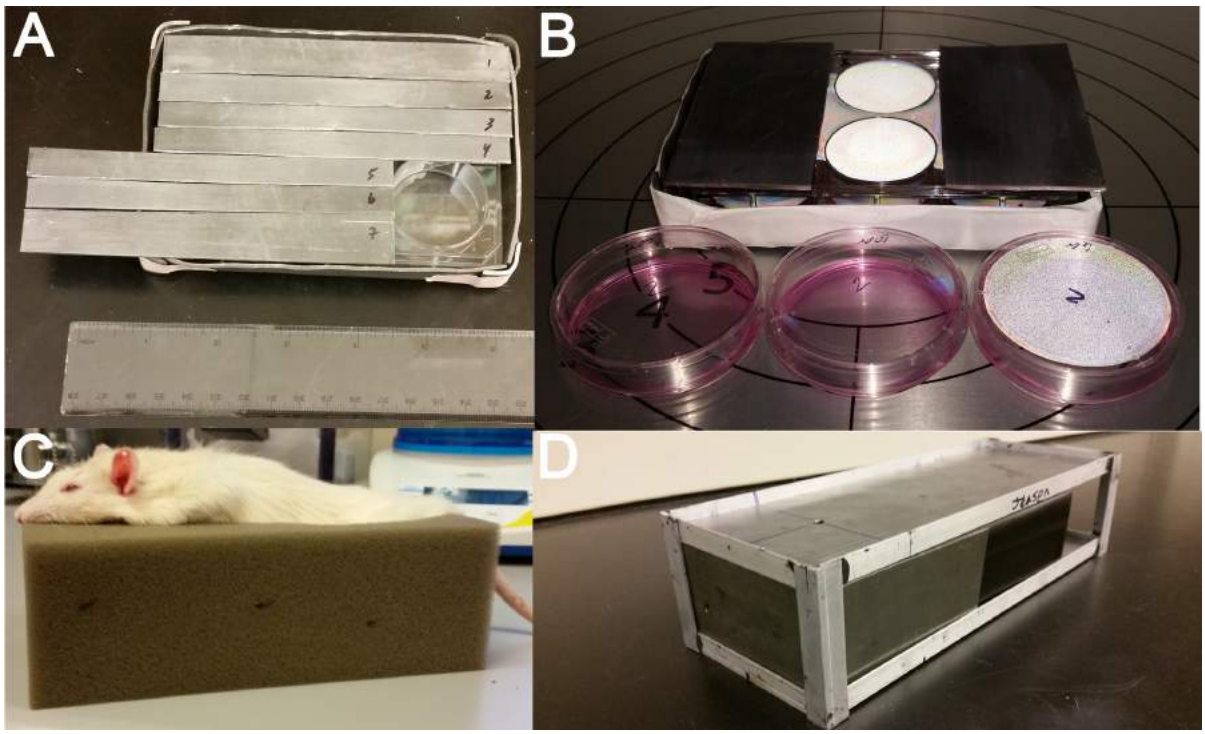

FIGURE 2.2: Devices for *in vitro* and *in vivo* stereotactic radiation delivery

A) Custom built lead shielding for 6-, 12-, 24- and 96-well plates allow for stereotactic radiation to desired wells. Shielding of culture wells was confirmed by dosiometry reading. B) Example of shielding setup in the radiation emitter during cell culture treatment. C) Custom foam padding customized for positioning of rodents during cranial radiosurgery. D) Custom lead shielding box designed for localized rodent cranial irradiation.

FIGURE 2.3: Evaluation of the dimensions of microvascularity using the local box-counting method.

A) To calculate the dimension of a symmetric square (*red*), smaller and smaller boxes (*black*) are created to fill the representative square. By dividing the width and length of the square by 1 box (r0 = 1), the area of the square can be covered by 1 box [N(r0) = 1]. By dividing the width and length by 2 boxes, the area of the square is covered by 4 boxes [N(r2) = 4]. Thus, the relationship of the box size (1/r) and number of boxes [N(r)] needed to cover the width and length is (1/r)2 = N(r) for a square. B) The graph of log 1/rn versus log(N(rn)) is shown. The slope of the curve represents the fractal dimension, db = 2. C) Infinitely repeating patterns (i.e., mathematical fractals) own a fractal dimension, which quantifies their geometrical complexity. For example, the Koch flake fractal pattern is a well-known sequence starting from a straight line and dividing the remaining segments in half before drawing a new bisection. The iteration of the process gives rise to the Koch curve, with a calculated dimension of 1.26. D) The box-counting method can be applied to microvascularity, with the assumption that the vasculature is an iteratively branching pattern (i.e., it is self-similar in a defined range of magnifications). The box-counting algorithm can be applied to the entire histological slide and to the hot spot region of the CD31-immunostained microvessels to compute the microvascular Loc bcD, which quantifies a single parameter, not just the density of the vessels, but also their size, shape, and pattern of distribution. Higher Loc bcD values signify the higher space-filling capacities of the vessels (e.g., a tumor with more tortuous and/or bigger microvessels). Figure is available in color online only.

Reprinted with permission from: Karsy M, Burnett B, Di Ieva A, Cusimano MD, & Jensen RL (2017) Microvascularization of Grade I meningiomas: effect on tumor volume, blood loss, and patient outcome. J Neurosurg:1-10. (83)

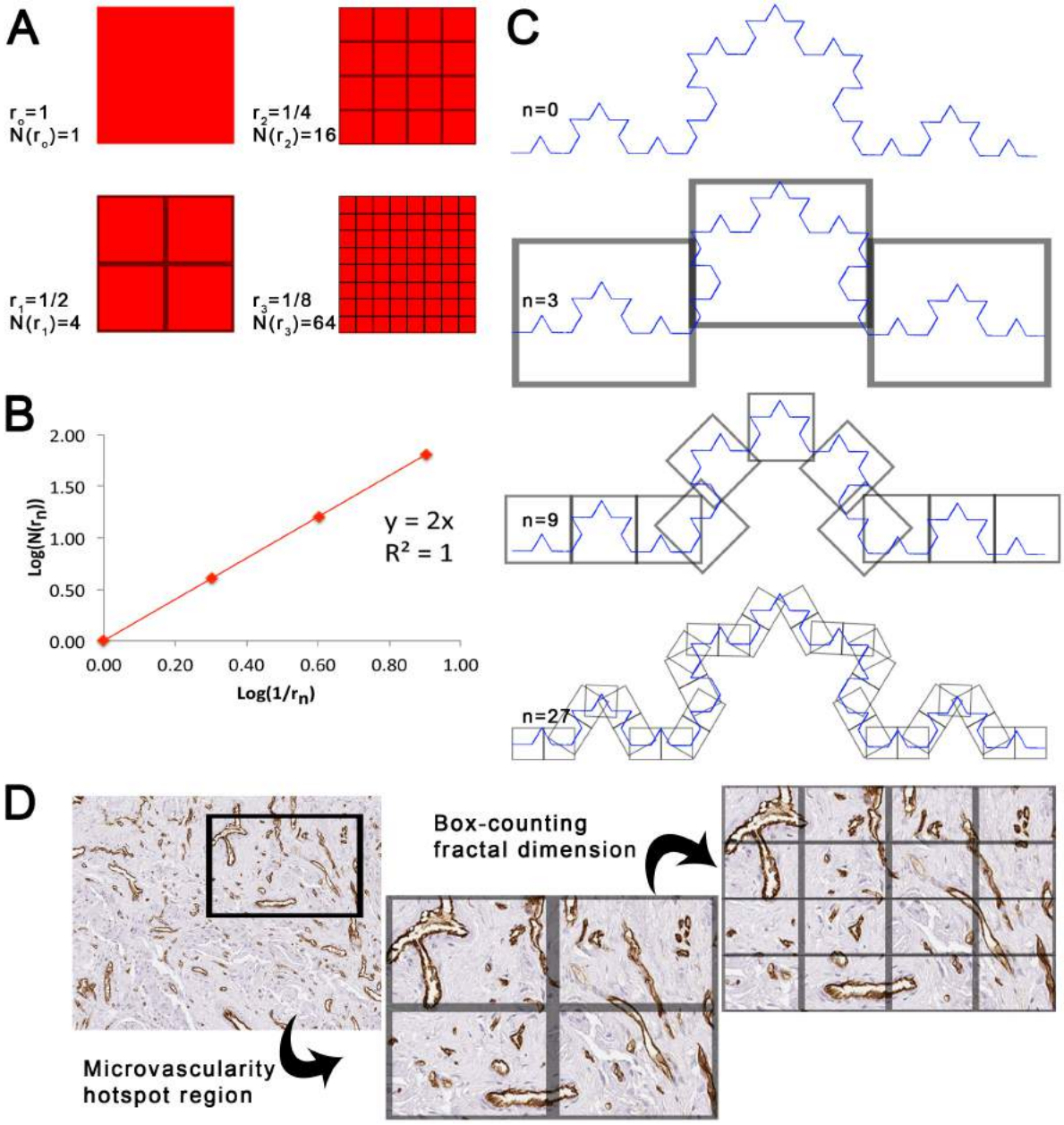
A
r_o=1
N(r_o)=1
r_2=1/4
N(r_2)=16
r_1=1/2
N(r_1)=4
r_3=1/8
N(r_3)=64
B
Log(N(r_n))
Log(1/r_n)
y = 2x
R^2 = 1
C
n=0
n=3
n=9
n=27
D
Box-counting
fractal dimension
Microvascularity
hotspot region

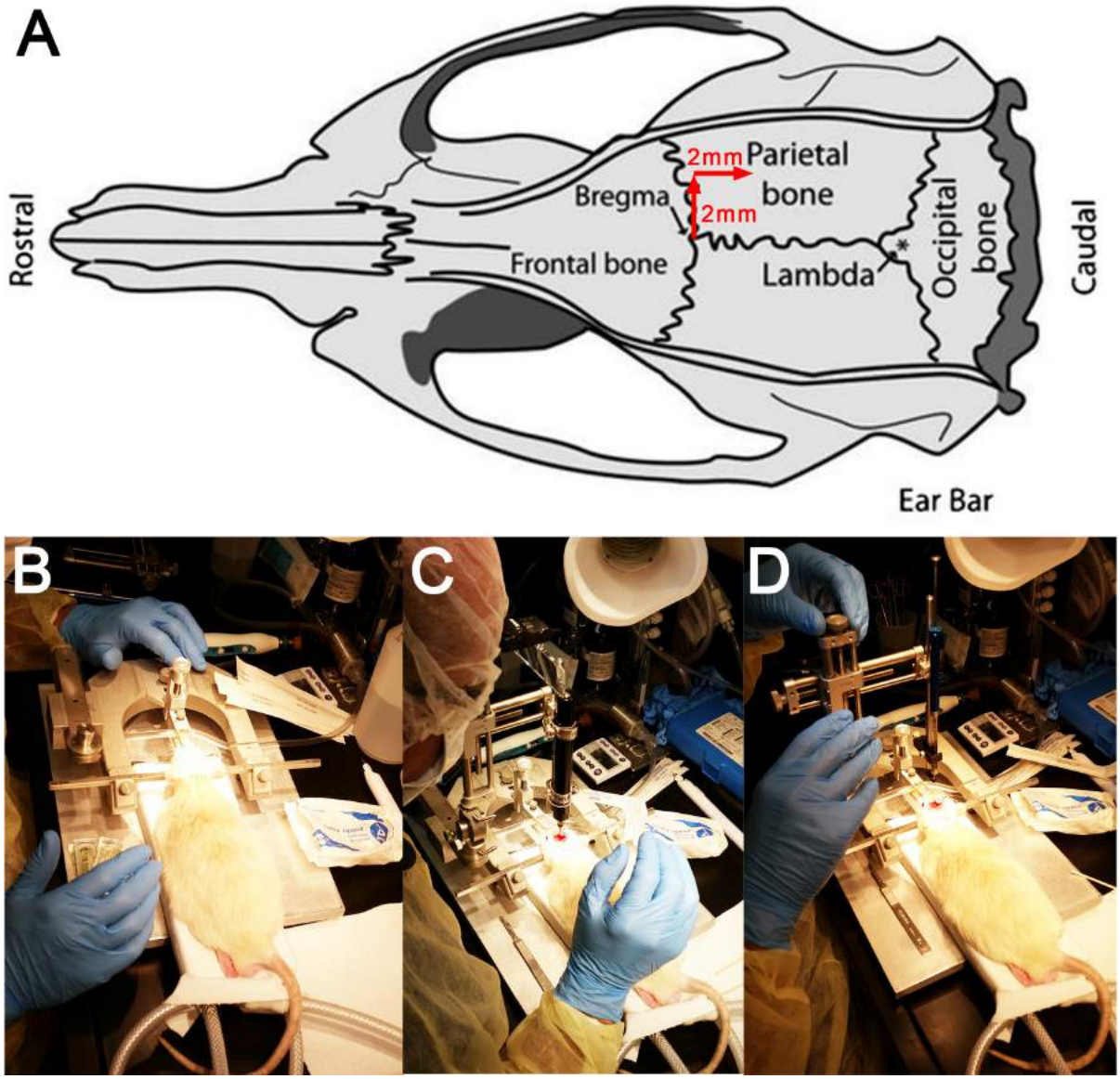

FIGURE 2.4: Stereotactic injection of rodent brain

A) Rodent sutures and cranial bones are shown with the intersection of the coronal and sagittal sutures marked as bregma. A burr hole is typically made 2mm laterally and 2mm posteriorly to the bregma. The depth is 3mm deep to the skull. B) Setup of the rodent in the stereotactic head frame is shown with a bite block for the teeth, a funnel to deliver anesthesia while on the frame, and ear prongs to maintain the head. A heated pad is placed under the animal. C) After incision and dissection, a microdrill is positioned at the burr hole site. D) Injection of the cells (8µl total volume, 1.5-3x10^5 cells total) via the Hamilton syringe and needle are shown.

CHAPTER 3

RESULTS

3.1 Clinical evaluation of HIF1α

Previous studies by Jensen et al. helped to elucidate the utility of microvascular density in identifying meningioma grade in clinical samples (15). We evaluated microvascular density, using both traditional and novel fractal-based approaches, of quantification in grade I meningiomas and correlated these findings to intraoperative parameters (83). Evaluation of the 207 included patients with grade I meningiomas showed a mean ± SD age of 55.4±14.8 years, with 63 (30.4%) male patients (Table 3.1). Mean EBL was 343.1±449.6 ml. Tumor volume calculation (21.63±33.28 ml) and measured volume (27.31±37.18 ml) showed good correlation (R=0.997, p=0.0001). Mean anteroposterior, lateral, and depth dimensions were 3.4±1.7, 2.8±1.6, and 2.7±1.6 cm, respectively. Mean OS was 124.1±64.0 months, mean PFS was 115.9±63.9 months, and at 6 months only one patient (0.5%) demonstrated progression.

A summary of vascularity assessments is provided in Table 3.2. Mean percentage of total field (± SD) for MIB index was 2.5±4.3, and mean microvascularity (%, ± SD) measured by vWF, CD31, and CD105 was 73.1±69.8, 18.2±12.1, and 13.4±8.0, respectively. The fractal-based microvascularity measure Loc bcD was 1.1±0.1. Mean expression of VEGF was 2.4±1.2, HIF-1 was 2.0±1.4, GLUT1 was 2.0±1.1, and CA-IX

was 2.5±1.3. Bivariate linear correlation showed significant correlation among microvascularity measures, automated fractal-based quantitation, and gene expression patterns (Table 3.3).

3.2 Evaluation of tumor size

The relationships among various measures of microvascularity and tumor size and biology were evaluated by T-test or Chi-square test (Table 3.4). Patients with tumors <3 cm tended to be slightly younger than patients with tumors ≥3 cm (53.1±13.6 vs. 56.9±15.2 years, p=0.07). Patients with smaller tumors were less likely to be male (14.6 vs. 40.8%, p=0.0001), had significantly lower EBL (185.4±197.2 vs. 446.5±532.2 ml, p=0.0001) and smaller tumor volume (29.4±23.5 vs. 33.9±38.1 ml, p=0.0001), and had lower MIB index (1.7±1.7 vs. 3.0±5.4, p=0.03), vWF (54.1±52.4 vs. 85.6±76.9, p=0.001), and HIF-1 expression (2.2±1.4 vs. 1.4±1.3, p=0.004). In addition, significantly lower mortality (17.1 vs. 30.4%, p=0.03) was also observed in patients with smaller tumors.

Kaplan-Meier survival analysis with Log rank test was performed with a tumor size cutoff of 3 cm (Figure 3.1). There was no difference in PFS related to tumor size (tumors <3 cm=180.9±9.0 vs. ≥3 cm=166.0±8.3 months, p=0.16); however, a significantly worse OS was seen in patients with tumors ≥3 cm (199.9±7.6 vs. 180.8±8.1 months, p=0.05).

Multivariate logistic regression was used to evaluate the contributors to larger tumor size (Table 3.5). Using a variable enter-method regression model for variables with p<0.1 on univariate linear regression analysis, sex (Odds ratio [OR]=3.75, 95% confidence interval [CI]=1.75, 8.00, p=0.001), MIB (OR=1.14, 95% CI=1.00, 1.31,

p=0.05), vWF (OR=1.01, 95% CI=1.00, 1.01, p=0.01), and HIF-1 (OR=1.54, 95% CI=1.22, 1.94, p=0.0001) were significant predictors of greater tumor size.

3.3 Linear regression analysis of EBL

Univariate and multivariate linear regression analysis were performed to identify predictors of EBL (Table 3.6). Univariate linear regression analysis showed EBL could be predicted by age (ρ=0.16, p=0.021), sex (ρ=0.198, p=0.004), calculated tumor volume (ρ=0.415, p=0.0001), vWF (ρ=0.229, p=0.006), and CD31 (ρ=0.321, p=0.006); however, multivariate linear regression analysis showed that only vWF remained significant (β=0.363, p=0.01).

3.4 Analysis of survival

We evaluated which factors might be used to predict disease progression (PFS) or death (OS) by T-test and Chi-squared analysis (Table 3.7). Younger patients had significantly longer time to disease progression (p=0.0001) and longer survival (p=0.0001). Similarly, those with lower EBL had longer PFS (p=0.0033) and OS (p=0.003). Univariate and multivariate linear regression analysis showed that MIB index had good correlation with PFS (ρ=-0.2, p=0.02) and OS (ρ=-0.2, p=0.03) on univariate linear regression analysis and was further explored as a prognostic marker (Table 3.8). No other factor was predictive of improved PFS and OS except for the correlation of CD105 with OS by multivariate analysis (β=0.4, p=0.009)

Due to the potential for a lead-time bias in identifying covariates, a Cox proportional hazards model was used to evaluate key factors predictive of PFS and OS (Table 3.9). Factors were selected for a model based on their significance ($p<0.05$) during

univariate and/or multivariate linear regression analysis. Age was a significant factor predicting a modest increase in PFS (OR: 1.05; 95% CI: 1.01, 1.09; p=0.007) and OS (OR: 1.12; 95% CI: 1.05, 1.18; p=0.0001). Sex, CD105, and HIF-1 expression did not show a significant impact on risk of PFS or OS. In addition, MIB was not associated with an increase in the risk of disease progression (OR: 1.08; 95% CI: 0.99, 1.19; p=0.08).

3.5 Threshold values for survival analysis

An ROC curve was used to evaluate the correlation of various microvascularity measurements and PFS and OS (Figure 3.2). Age demonstrated good discriminative ability for delineating PFS, while MIB, CD105, and HIF-1 showed an intermediate discriminative ability. Sex did not discriminate PFS well. Age also showed a strong discriminative ability for OS, while CD105 and HIF-1 showed an intermediate ability. MIB and sex did not show good discrimination of OS. An MIB cutoff was further evaluated in predicting PFS and OS (Table 3.10, Figure 3.1C,D). A MIB cutoff of ≥3 yielded a 36% sensitivity and 82.5% specificity for PFS and 11.8% sensitivity and 72.9% specificity for OS. Use of a MIB cutoff of ≥3 showed a significant difference in PFS (p=0.05) but not OS (p=0.56) by Kaplan-Meier survival with log-rank test (Figure 3.1). For a MIB of ≥3 compared with <3, there was a significant difference in PFS (140.1±11.7 vs. 179.5±7.0 months, p=0.05) but not OS (172.7±11.8 vs. 192.5±6.6 months, p=0.56). Decision-tree analysis of all microvascularity-related variables in predicting PFS and OS yielded significant results only for MIB index (results not shown).

3.6 Analysis of primary meningioma samples

Analysis of meningioma cell sample proliferation rates were evaluated by cell counting (Figure 3.3A). IOMM-LEE, JEN, and GAR cells showed more rapid proliferation than SAM, MCT, and BSH cells. Cell doubling times of 19.5, 38.9, 45.2, and 213.2 hours were identified using an exponential cell growth model for IOMM-LEE, JEN, GAR, and MCT cells, respectively. Doubling times for SAM and BSH cells could not be reliably calculated. Prior growth rate results utilized a linear relationship between cell count and time. IOMM-LEE cells showed an *in vitro* doubling time of 20 hours and *in vivo* flank model growth rate of 12 days. *In vitro* doubling times and *in vivo* flank model growth rates for GAR cells were 40 hours and 10 days and for JEN cells were 65 hours and 15 days, respectively.

3.7 Impact of cell density on radiation responsiveness

Cell responsiveness to radiation was then evaluating using a dilutional assay (Figure 3.3B-F). Cells showed similar rates of proliferation, which were dependent on the number of cells plated, when comparing cell confluency at day 6 with that at day 3. Cell confluency also played a role in responsiveness to radiation. GAR, IOMM-LEE, and Jen showed reduced cell confluency at day 6 compared with day 3 at all plated cell concentrations. In addition, wells with low numbers (10–500) of seeded cells did not withstand higher doses of radiation. The ratio of cell viability between days 3 and 2 for IOMM-LEE cells confirmed the pattern of increased viability for higher number of plated cells. These results suggested that cell–cell contact and high cell density affected response to radiation. Previous studies have supported the dependence of reactive oxygen species and radiation sensitivity on cell density in a variety of neural precursor cell types.

3.8 Impact of *HIF1A* knockout and hypoxia on radiation responsiveness

To evaluate the impact of *HIF1A* knockout and hypoxia on meningioma responsiveness to radiation, a single cell line with (GAR1589) and without (GAR) *HIF1A* knockout was utilized. Preliminary results did not show a significant difference in cell counts after single doses of 2, 5 or 10Gy radiation for GAR ($p=0.99$, one-way ANOVA) or GAR1589 ($p=0.40$, one-way ANOVA) cells (Figure 3.4A, B). However this method did not offer significant sensitivity to detect the impact of since fraction radiation treatments. Cell luminescence offered improved resolution of cell viability differences with culturing in normoxic environments (Figure 3.4C). Cell viability for GAR1589 cells was reduced compared with GAR cells at control ($p=0.0001$, T-test), 2 Gy ($p=0.05$), and 10 Gy ($p=0.02$) treatment conditions. No difference in cell viability was observed with 20-Gy ($p=0.07$) treatments. Although GAR cells showed decreased viability with increased radiation dose, the decrease was only significant at 20 Gy ($p=0.028$, one-way ANOVA). GAR1589 cells surprisingly showed increased cell viability at 2 Gy ($p=0.022$, one-way ANOVA). These results suggest that HIF1A played a role in resistance to radiation and knockdown reduced overall viability compared with wild-type conditions.

Cell treatments in hypoxic conditions were used to evaluate responsiveness to radiation (Figure 3.4D). A significant difference between GAR and GAR1589 cell viability was seen at 2 Gy ($p=0.05$, T-test) but not for control ($p=0.9$), 4 Gy ($p=0.3$), or 10 Gy ($p=0.4$) in hypoxic conditions. Increased cell viability was seen for GAR cells with higher-dose radiotherapy but the increase was significant only at 4 Gy ($p=0.022$, one-way ANOVA). No difference among GAR1589 treatment conditions was observed ($p=0.361$). Overall differences between GAR and GAR1589 were reduced during hypoxic conditioning at various doses of radiation. Increased cell viability at low radiation doses

was only seen for GAR cells. This result supports the known importance of oxygenated environments in impacting reactive oxygen species and sensitivity to radiation.

3.9 Impact of radiation fractions and *HIF1A* knockout

Current treatment regimens for aggressive lesions can involve fractionated radiotherapy to delivery higher doses than single whole-brain or stereotactic doses. GAR and GAR1589 cells were counted over time with or without daily 2-Gy radiation fractions (Figure 3.5A-D). A significant increase in GAR cell proliferation was seen after 4 and 5 days of continuous culture compared with control ($p=0.0001$, one-way ANOVA) (Figure 3.5A,B). A significant increase in GAR1589 cells was seen at 3, 4, and 5 days compared with control ($p=0.0001$). No significant difference in cell counts was seen for GAR ($p=0.081$) or GAR1589 ($p=0.06$) cells that received daily 2-Gy radiation fractions. Cell doubling times were calculated as 25.0 days for GAR cells, 40 days for GAR1589 cells, and 365 days for GAR cells receiving 2-Gy daily radiation; no doubling time could be identified for GAR1589 cells receiving radiation. During hypoxic treatments and cell counting, a significant increase in cell counts was only seen for GAR cells under hypoxic conditions ($p=0.03$) (Figure 3.5C,D). No cell proliferation differences were seen between GAR1589 cells in hypoxia or GAR and GAR1589 cells receiving radiation in hypoxia. These results support that loss of HIF1A reduces resistance to radiation and hypoxic microenvironments in meningioma cells.

Evaluation of cell treatments using cell viability supported these results (Figure 3.5E,F). GAR1589 cell viability was significantly lower at baseline than GAR cell viability in normoxia ($p=0.01$, t-test). No difference in cell viability was observed when 1 or 2 fractions of 2 Gy were applied. A significant difference between GAR and

GAR1589 cells was then seen at 3 fractions of 2 Gy (p=0.01). GAR cells did not show an appreciable reduction in viability with radiation (p=0.26, one-way ANOVA) whereas GAR1589 cells were significantly reduced after 3 fractions (p=0.007). During hypoxic conditions, no difference in cell viability was seen between GAR and GAR1589 at 0 (p=0.14, t-test), 1 (p=0.94), 2 (p=0.08), or 3 fractions (p=0.2). Treatments also did not reduce viability over time for GAR (p=0.18, one-way ANOVA) or GAR1589 (p=0.097) fractionated treatments. These results offer support for the hypothesis that the presence of HIF1A confers resistance to radiation whereas hypoxic environments abate radiation sensitivity.

3.10 Evaluation of apoptosis with radiation and *HIF1A* knockout

To identify potential mechanisms for radiation sensitivity in GAR cells, apoptosis was evaluated (Figure 3.6). In normoxia, the number of apoptotic cells was significantly higher in GAR1589 cells at control (p=0.001, t-test), 2 Gy (p=0.001), and 4 Gy (p=0.01) but not 10 Gy (p=0.31) when compared with GAR cells (Figure 3.6A). There was also more cell apoptosis at 10 Gy for both GAR and GAR1589 cells compared with lower-dose treatments, but only GAR1589 cells were significantly different from controls (p=0.006, one-way ANOVA; control vs. 10 Gy, p=0.008). During hypoxic treatments, no significant difference was observed between GAR and GAR1589 cells for control (p=0.07), 2 Gy (p=0.06), 4 Gy (p=0.15) or 10 Gy (p=0.31) treatments (Figure 3.6B). These results suggest an overall increase in apoptosis for GAR1589 cells, indicating that HIF1A is protective during cell culture. In addition, these cells were sensitive to radiation at lower doses, suggesting HIF1A is protective against radiation-induced apoptosis. Finally, hypoxia abated many of the differences between GAR and GAR1589 cells,

corroborating the conclusion that oxygen tension plays a role in resistance to radiation for GAR cells.

3.11 Live cell evaluation of cell proliferation in meningiomas

GAR and GAR1589 cells were plated at 50% confluency, evaluated by hourly imaging, and analyzed by automated methods. GAR cells showed an initial drop in cell confluency after a single fraction of 10Gy or 20Gy radiation followed by slower growth curve from 2-5 days and then plateauing at a lower confluency thereafter (Figure 3.7A). GAR1589 cells also showed an initial drop in cell confluency after a single 10Gy or 20Gy radiation fraction but continued to show slow cell proliferation from day 2 until 8 days (Figure 3.7B). No cell confluency plateau was seen. The impact of radiation after adjustment for baseline cell proliferation rates showed that radiation equally inhibited both GAR and GAR1589 cell lines up to 100 days. However lower proliferative capacity was seen thereafter for GAR1589 cells (Figure 3.7C,D). In addition, GAR1589 cells showed greater differentiation into cells resembling astrocytes with extended processes, as well as cell apoptosis, with membrane blebbing, constriction and detachment (Figure 3.7E). Representative video snapshots with confluency masks were generated for all treatment conditions (results not shown).

3.12 Colony formation assay and radiation in meningioma

A colony formation assay was used to evaluate the impact of radiotherapy. Dark field microscopy (Figure 3.8A) and light microscopy (Figure 3.8B) were used to evaluate response of GAR and GAR1589 cells to 2Gy and 10Gy of single-fraction radiation. Evaluation of % total area after dark field microscopy did not show any significant

difference after radiation (p=0.12, one-way ANOVA). However, evaluation after crystal violet staining showed a significant in cell % total area (p=0.0001, one-way ANOVA) and colony count (p=0.0001, one-way ANOVA) (Figure 3.8C-E). Tukey post-hoc comparison showed a significant decrease in % total area for GAR cells at 2Gy (p=0.007) and 10Gy (p=0.011) as well as GAR1589 cells at 2Gy (p=0.003) but not 10Gy (p=0.074) (Figure 3.8D). For colony count, reduction for GAR cells at 2Gy (p=0.001) and 10Gy (p=0.002) as well as GAR1589 cells at 2Gy (p=0.0001) and 10Gy (p=0.0001) was seen (Figure 3.8E).

3.13 *In vivo* imaging of hypoxia

Evaluation of multimodal imaging of proliferation and hypoxia was performed in a syngenic F98 rodent glioma model using bioluminescence, MR, FMISO PET and FLT PET imaging. Bioluminescence imaging showed increased tumor growth over a 1-week period of time up to 3 weeks (Figure 3.9A). Concomitant MR, FMISO and FLT imaging showed initial increase in FLT that correlated with MRI intensity at day 6/7 followed by increased FMISO expression, highest at day 20/21 (Figure 3.9B). This suggested that hypoxia followed increased tumor size and proliferation. Quantitated imaging reflected collinearly, increased MRI, FLT, and FMISO, which differed for individual animals (Figure 3.10A,B).

TABLE 3.1: Summary of the baseline variables of the patients with Grade I meningiomas

Variable	Value
No. of patients	207
Age, yrs	55.4 ± 14.8
No. of male patients (%)	63 (30.4)
EBL, ml	343.1 ± 449.6
Tumor vol calculation, ml	21.6 ± 33.2
Measured vol, ml	27.3 ± 37.2
Anteroposterior dimension, cm	3.4 ± 1.7
Lateral dimension, cm	2.8 ± 1.6
Depth, cm	2.7 ± 1.6
Maximum dimension, cm	3.6 ± 1.9
OS, mos	124.1 ± 64.0
PFS, mos	115.9 ± 63.9
6-mo PFS, %	0.5

Values are shown as the mean ± SD unless otherwise indicated.

Reprinted with permission from: Karsy M, Burnett B, Di Ieva A, Cusimano MD, & Jensen RL (2017) Microvascularization of Grade I meningiomas: effect on tumor volume, blood loss, and patient outcome. J Neurosurg:1-10. (83)

TABLE 3.2: Summary of the immunohistological variables of the patients with Grade I meningiomas

Variable	Value
No. of patients	207
MIB index, % of field	2.5 ± 4.3
vWF, % of field	73.1 ± 69.8
CD31, % of field	18.2 ± 12.1
CD105, % of field	13.4 ± 8.0
Loc bcD*	1.1 ± 0.1
VEGF expression*	2.4 ± 1.2
HIF-1 expression*	2.0 ± 1.4
GLUT-1 expression*	2.0 ± 1.1
CA-IX expression*	2.5 ± 1.3

Values are shown as the mean ± SD unless otherwise indicated.

* Scored from 0-4 depending on the number of stained cells in a field (0, 0%–25%; 1, 25%–50%; 2, 50%–75%; 3, 75%–100%; and 4, 100%).

Reprinted with permission from: Karsy M, Burnett B, Di Ieva A, Cusimano MD, & Jensen RL (2017) Microvascularization of Grade I meningiomas: effect on tumor volume, blood loss, and patient outcome. J Neurosurg:1-10. (83)

TABLE 3.3: Immunohistological assessment of vascularity in meningiomas

Corr. coeff. **P-val**	**MIB**	**vWF**	**CD31**	**CD105**	**LocbcD**	**Tumor vol.**	**VEGF**	**HIF-1**	**GLUT1**	**CA-IX**
MIB	1	**0.26**	-0.065	0.097	0.14	**0.17**	-0.06	0.2	0.002	-0.02
	.	**0.0001**	0.59	0.44	0.24	**0.016**	0.42	0.8	0.97	0.83
vWF		1	**0.46**	0.15	0.30	**0.34**	0.04	-0.02	-0.03	-0.008
		.	**0.0001**	0.24	0.009	**0.0001**	0.57	0.76	0.69	0.91
CD31			1	**0.33**	**0.29**	**0.24**	0.13	-0.2	-0.07	-0.11
			.	**0.007**	**0.015**	**0.038**	0.26	0.88	0.57	0.37
CD105				1	0.11	0.21	0.04	-0.03	**0.31**	0.07
				.	0.39	0.095	0.76	0.79	**0.01**	0.56
LocbcD					1	0.17	-0.14	-0.09	0.05	0.03
					.	0.14	0.25	0.45	0.66	0.81
Tumor vol.						1	-0.034	**0.19**	0.41	0.06
						.	0.63	**0.007**	0.56	0.37
VEGF							1	**0.17**	**0.25**	**0.29**
							.	**0.02**	**0.0001**	**0.0001**
HIF-1								1	**0.47**	**0.38**
								.	**0.0001**	**0.0001**
GLUT1									1	**0.45**
									.	**0.0001**
CA-IX										1
										.

Reprinted with permission from: Karsy M, Burnett B, Di Ieva A, Cusimano MD, & Jensen RL (2017) Microvascularization of Grade I meningiomas: effect on tumor volume, blood loss, and patient outcome. J Neurosurg:1-10. (83)

TABLE 3.4: Analysis of variables affected by the tumor size of Grade I meningiomas

Variable	Tumor Size		p Value
	< 3 cm	**≥ 3 cm**	
No. of patients	137	70	
Age, yrs	53.1 ± 13.6	56.9 ± 15.2	0.07
No. of male patients (%)	12 (14.6)	41 (40.8)	**0.0001**
EBL, ml	185.4 ± 197.2	446.5 ± 532.2	**0.0001**
Tumor vol, ml	29.4 ± 23.5	33.9 ± 38.1	**0.0001**
MIB-1, % of field	1.7 ± 1.7	3.0 ± 5.4	**0.03**
vWF, % of field	54.1 ± 52.4	85.6 ± 76.9	**0.001**
CD31, % of field	16.1 ± 11.2	19.3 ± 12.5	0.29
CD105, % of field	10.9 ± 5.9	14.6 ± 8.6	0.07
Loc bcD*	1.1 ± 0.2	1.2 ± 0.1	0.09
VEGF expression*	2.3 ± 1.2	2.5 ± 1.2	0.89
HIF-1 expression*	2.2 ± 1.4	1.4 ± 1.3	**0.004**
GLUT-1 expression*	2.1 ± 2.0	1.1 ± 1.1	0.65
CA-IX expression*	2.6 ± 1.3	2.4 ± 1.2	0.26
PFS, mos.	119.2 ± 59.9	113.7 ± 66.6	0.54
No. w/ progression (%)	22 (26.8)	48 (38.4)	0.09
OS, mos.	130.4 ± 58.5	120 ± 67.3	0.25
No. deceased (%)	14 (17.1)	38 (30.4)	**0.03**

Values are shown as the mean ± SD unless otherwise indicated.

* Scored from 0-4 depending on the number of stained cells in a field (0, 0%–25%; 1, 25%–50%; 2, 50%–75%; 3, 75%–100%; and 4, 100%).

Reprinted with permission from: Karsy M, Burnett B, Di Ieva A, Cusimano MD, & Jensen RL (2017) Microvascularization of Grade I meningiomas: effect on tumor volume, blood loss, and patient outcome. J Neurosurg:1-10. (83)

TABLE 3.5: Logistic regression of predicting tumor size in Grade I meningiomas

Variable	OR	95% CI	p-Value
Sex	3.75	1.75–8.00	0.001
MIB-1, % of field	1.14	1.00–1.31	0.05
vWF, % of field	1.01	1.00–1.01	0.01
HIF-1 expression	1.54	1.22–1.94	0.0001

Reprinted with permission from: Karsy M, Burnett B, Di Ieva A, Cusimano MD, & Jensen RL (2017) Microvascularization of Grade I meningiomas: effect on tumor volume, blood loss, and patient outcome. J Neurosurg:1-10. (83)

TABLE 3.6: Factors predictive of EBL during meningioma resection

Variable	Univariate		Multivariate*	
	ρ	p Value	β	p Value
Age, yrs	0.16	**0.021**	0.056	0.66
Male	0.2	**0.004**	0.12	0.35
Tumor vol, ml	0.42	**0.0001**	0.19	0.16
MIB-1, % of field	0.014	0.84		
vWF, % of field	0.23	**0.001**	0.36	**0.01**
CD31, % of field	0.32	**0.006**	0.069	0.64
CD105, % of field	0.16	0.18	-0.071	0.59
Loc bcD	0.15	0.22	-0.02	0.87
VEGF expression	0.10	0.15	-0.037	0.78
HIF-1 expression	-0.02	0.75		
GLUT-1 expression	-0.03	0.67		
CA-IX expression	0.09	0.22	0.029	0.82

* The multivariate model included the univariate variables with $p < 0.25$, $R = 0.486$, and $p = 0.073$.

Reprinted with permission from: Karsy M, Burnett B, Di Ieva A, Cusimano MD, & Jensen RL (2017) Microvascularization of Grade I meningiomas: effect on tumor volume, blood loss, and patient outcome. J Neurosurg:1-10. (83)

TABLE 3.7: Analysis of variables predicting progression-free and overall survival for patients with grade I meningiomas

	Progression			**Survival**		
	No N=137	**Yes N=70**	**P-value**	**Yes N=155**	**No N=52**	**P-value**
Age (years)	52.1±13.1	61.8±15.8	**0.0001**	51.1±13.6	67.0±11.7	**0.0001**
No. of male patients (%)	39 (28.5)	24 (34.3)	0.39	44 (28.4)	19 (36.5)	0.27
EBL (ml)	295.6±418.6	425.9±498.0	**0.033**	289.3±399.1	503.3±548.3	**0.003**
Tumor vol. (ml)	18.9.0±30.0	27.1±38.4	0.09	20.03±34.0	26.4±30.9	0.23
MIB	2.5±5.0	2.4±2.6	0.79	2.6±4.9	2.0±2.1	0.39
vWF	71.4±64.0	76.5±80.4	0.62	71.0±64.2	79.3±84.9	0.46
CD31	19.2±13.8	16.7±9.0	0.39	19.5±13.4	15.0±7.3	0.15
CD105	12.3±7.6	15.0±8.4	0.19	12.4±7.4	16.0±9.1	0.11
Loc bcD	1.1±0.2	1.2±0.1	0.66	1.1±0.2	1.1±0.1	0.57
VEGF	2.3±1.2	2.5±1.3	0.50	2.3±1.2	2.5±1.3	0.48
HIF-1	2.0±1.4	2.0±1.5	0.84	1.9±1.4	2.1±1.5	0.29
GLUT1	1.9±1.1	2.2±1.1	0.08	1.9±1.1	2.4±1.2	**0.02**
CA-IX	2.4±1.3	2.6±1.3	0.31	2.4±1.3	2.6±1.3	0.50
PFS (months)	132.6±60.3	83.3±58.4	**0.0001**	128.2±60.2	79.3±61.2	**0.0001**
OS (months)	134.4±58.7	103.9±69.4	**0.001**	138.2±58.6	81.9±61.4	**0.0001**
No. deceased (%)	0 (0)	52 (74.3)	**0.0001**	0 (0)	52 (100)	

Reprinted with permission from: Karsy M, Burnett B, Di Ieva A, Cusimano MD, & Jensen RL (2017) Microvascularization of Grade I meningiomas: effect on tumor volume, blood loss, and patient outcome. J Neurosurg:1-10. (83)

TABLE 3.8: Univariate and multivariate analysis of variables predicting progression-free and overall survival for patients with grade I meningioma**s**

Survival time	**Progression-free**				**Overall**			
Analysis	**Univariate**		**Multivariate[a]**		**Univariate**		**Multivariate[b]**	
	ρ	**p-value**	**β**	**p-value**	**ρ**	**p-value**	**β**	**p-value**
Age	-0.15	**0.04**	-0.08	0.84	-0.3	0.72		
Male sex	-0.07	0.36			-0.9	0.27		
EBL	-0.02	0.78			0.1	0.23	-0.1	0.34
Tum. vol.	-0.1	0.19	-0.41	0.47	-0.02	0.78		
MIB	-0.2	**0.02**	-0.22	0.65	-0.2	**0.03**	-0.07	0.63
vWF	-0.08	0.28			-0.05	0.55		
CD31	0.04	0.73			0.1	0.38		
CD105	0.06	0.67			0.4	**0.006**	0.4	**0.009**
Loc bcD	-0.07	0.57			-0.03	0.81		
VEGF	0.05	0.50			0.09	0.29		
HIF-1	-0.2	**0.007**	-0.16	0.73	-0.2	**0.03**	-0.1	0.52
GLUT1	-0.1	0.09	1.13	0.10	-0.1	0.09	0.1	0.56
CA-IX	-0.09	0.25	-0.39	0.51	-0.1	0.15	-0.2	0.13

[a]Model, univariate variables with $p<0.25$, $R=0.82$, p-value=0.46
[b]Model, univariate variables with $p<0.25$, $R=0.24$, p-value=0.061

Reprinted with permission from: Karsy M, Burnett B, Di Ieva A, Cusimano MD, & Jensen RL (2017) Microvascularization of Grade I meningiomas: effect on tumor volume, blood loss, and patient outcome. J Neurosurg:1-10. (83)

TABLE 3.9: Time-to-event–dependent Cox proportional hazards model

	PFS			OS		
Variable	**OR**	**95% CI**	**p Value**	**OR**	**95% CI**	**p Value**
Age, yrs	1.05	1.01–1.09	**0.007**	1.12	1.05–1.18	**0.0001**
Sex, male	1.08	0.43–2.72	0.86	1.06	0.30–3.71	0.93
MIB-1, % of field	1.08	0.99–1.19	0.08	0.94	0.72–1.23	0.66
CD105, % of field	1.00	0.96–1.04	0.84	0.97	0.95–1.05	0.97
HIF-1 expression	1.18	0.89–1.58	0.25	1.13	0.81–1.58	0.49

Reprinted with permission from: Karsy M, Burnett B, Di Ieva A, Cusimano MD, & Jensen RL (2017) Microvascularization of Grade I meningiomas: effect on tumor volume, blood loss, and patient outcome. J Neurosurg:1-10. (83)

TABLE 3.10: Summary of cutoffs for progression-free and overall survival analysis

Cutoff	PFS Log-Rank P-value	OS Log-Rank P-value
MIB=1.1[a]	**0.014**	0.28
MIB=3[b]	**0.05**	0.56
MIB=5[c]	0.66	0.36

[a]PFS: sens 60%, spec 52.5%; OS: sens 47.1%, spec 45.8%
[b]PFS: sens 36%, spec 82.5%; OS: sens 11.8%, spec 72.9%
[b]PFS: sens 20%, spec 90%; OS: sens 0%, spec 81.2%

Reprinted with permission from: Karsy M, Burnett B, Di Ieva A, Cusimano MD, & Jensen RL (2017) Microvascularization of Grade I meningiomas: effect on tumor volume, blood loss, and patient outcome. J Neurosurg:1-10. (83)

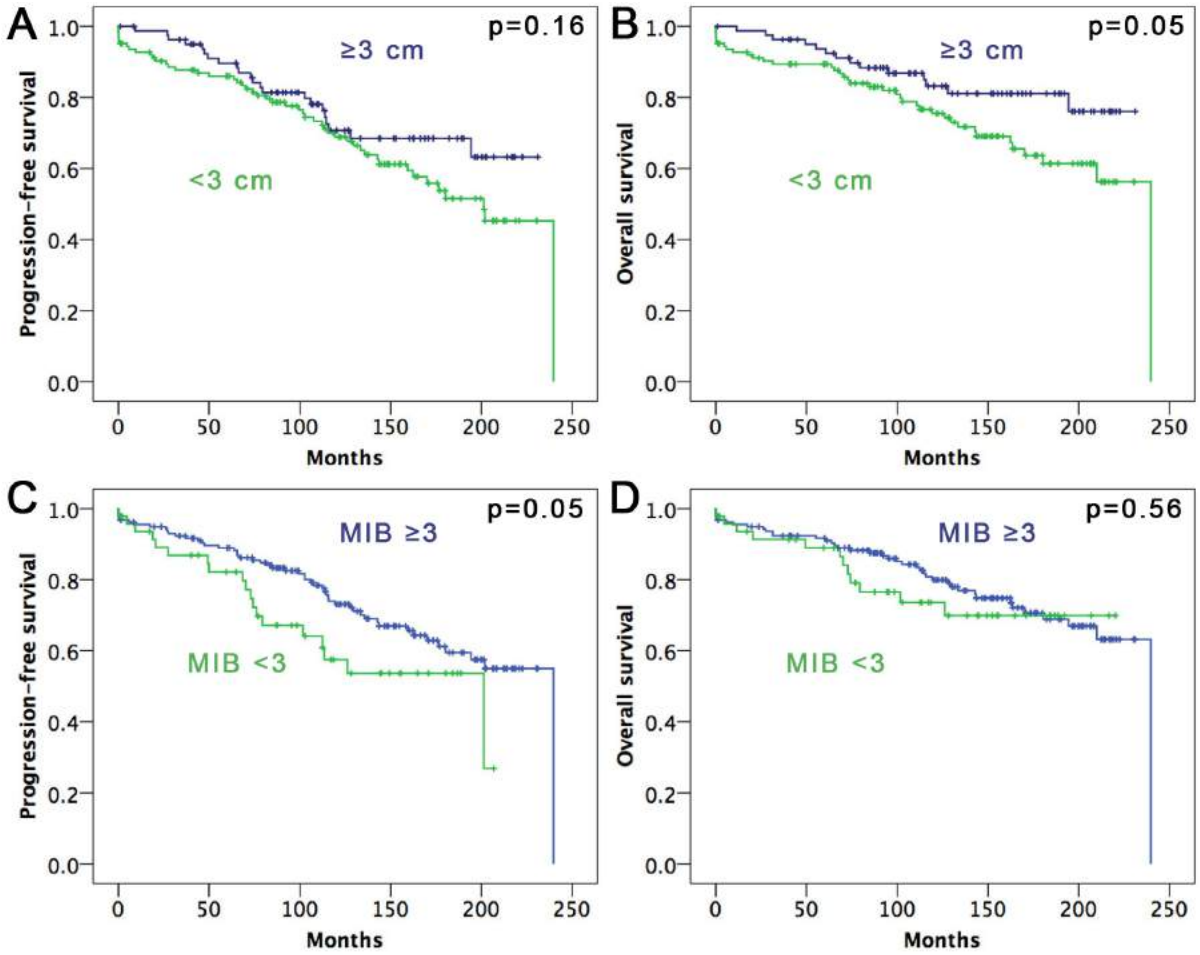

FIGURE 3.1: PFS and OS analysis using tumor size and the MIB-1 cutoff values for Grade I meningiomas.

Various cutoff values for tumor size and the MIB-1 index were used to investigate patient outcome. A) There was no significant difference in PFS (180.9 ± 9.0 months vs. 166.0 ± 8.3 months; p = 0.16) when comparing patients with tumors ≥ 3 cm or < 3 cm, but B) there was a significantly lower OS (199.9 ± 7.6 months vs. 180.8 ± 8.1 months; p = 0.05) for patients with larger tumors. C) Patients with an MIB-1 index of ≥ 3% had a significantly lower PFS (140.1 ± 11.7 months vs. 179.5 ± 7.0 months; p = 0.05) than those with an MIB-1 index < 3%, but D) there was no significant difference in OS (172.7 ± 11.8 months vs.192.5 ± 6.6 months; p = 0.56) between the 2 groups.

Reprinted with permission from: Karsy M, Burnett B, Di Ieva A, Cusimano MD, & Jensen RL (2017) Microvascularization of Grade I meningiomas: effect on tumor volume, blood loss, and patient outcome. J Neurosurg:1-10. (83)

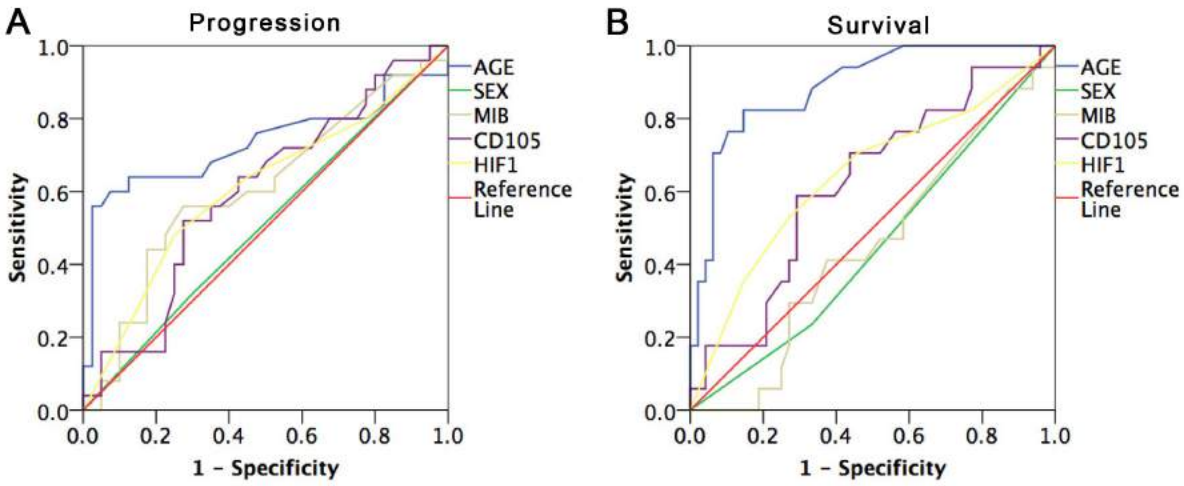

FIGURE 3.2: Receiver operating characteristics (ROC) curves of microvascularity measurements select specific cutoffs for predicting outcome in grade I meningiomas

A) Receiver operating characteristic (ROC) curves were used to select cutoff values for predicting progression-free survival (PFS). Age (p=0.002, AUC=0.73) showed the best ability in delineating cases bound to progress. MIB (p=0.14, AUC=0.61), CD105 (p=0.18, AUC=0.60), and HIF-1 (p=0.15, AUC=0.61) showed an intermediate ability to predict PFS. Sex (p=0.89, AUC=0.51) did not show significant predictive ability. B) ROC curves were used to select cutoff values for prediction of overall survival (OS). Age (p=0.0001, AUC=0.89) showed a strong discriminative ability, whereas CD105 (p=0.13, AUC=0.62) and HIF-1 (p=0.08, AUC=0.65) showed an intermediate ability, and sex (p=0.55, AUC=0.45) along with MIB (p=0.55, AUC=0.54) did not discriminate OS.

Reprinted with permission from: Karsy M, Burnett B, Di Ieva A, Cusimano MD, & Jensen RL (2017) Microvascularization of Grade I meningiomas: effect on tumor volume, blood loss, and patient outcome. J Neurosurg:1-10. (83)

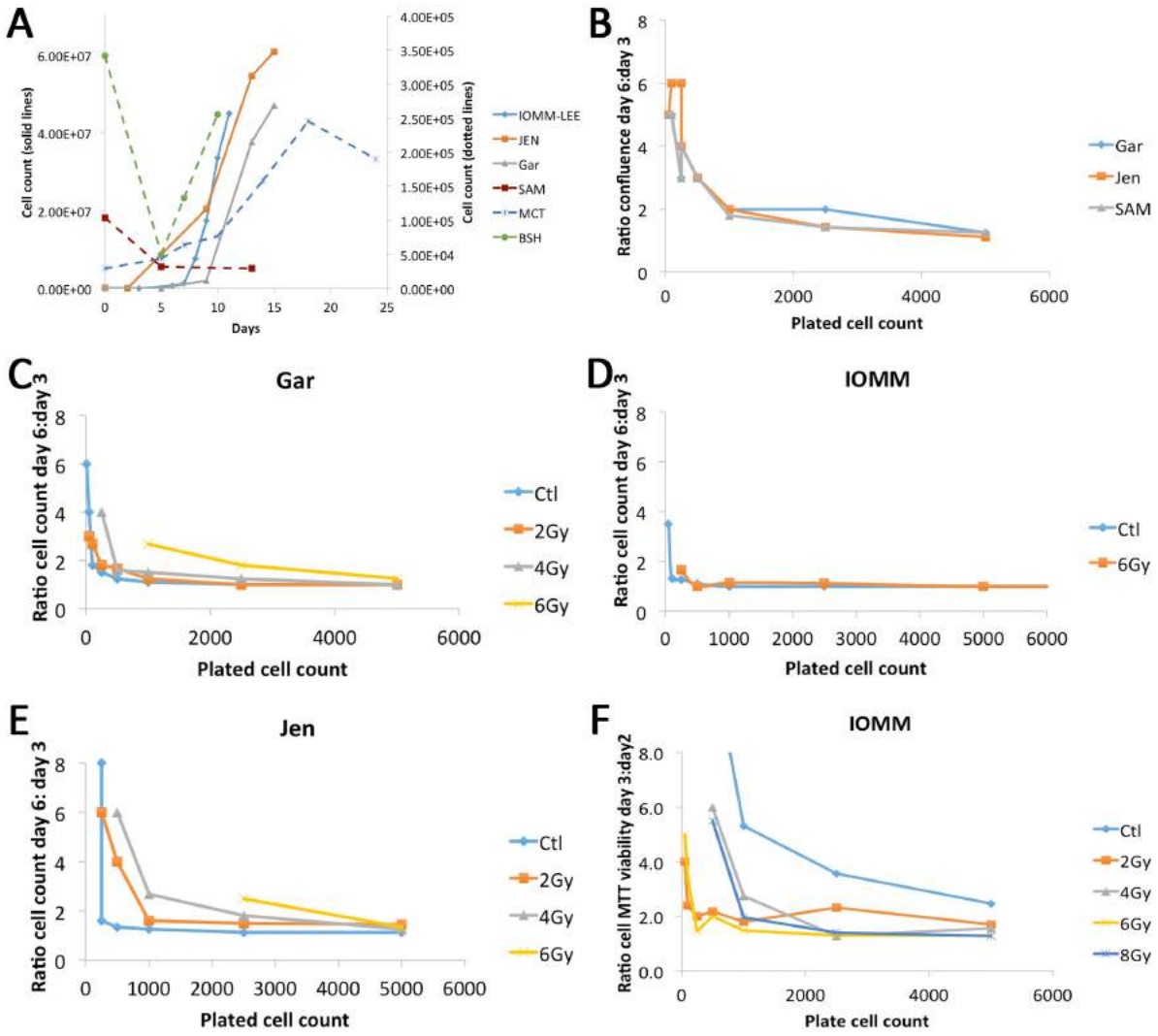

FIGURE 3.3: Cell proliferation rates and impact of cell density on radiation responsiveness

A) Proliferation rates for various meningioma cell lines were calculated by cell counting. Exponential modeling showed doubling times of 159.9, 23.6, 20.3, 6.9, 7.0, and 4.7 hours for IOMM-LEE, JEN, GAR, SAM, MCT, and BSH cells, respectively. Cell proliferation patterns were inconsistent for SAM, MCT, and BSH cells. Solid lines are measured on the left Y-axis, dotted lines are measured on the right Y-axis. B) The ratio of cell confluency for day 6 and day 3 was not appreciably different for GAR, JEN, and SAM lines. (C–E) Responsiveness to single radiation doses (2, 4, and 6 Gy) depending on cell density were evaluated for C) GAR, D) IOMM-LEE, and E) Jen cell lines. Low-density wells (10–500 cells) showed greater susceptibility to radiation at higher doses. E) MTT assay to evaluate IOMM-LEE cells showed similar increases in cell viability with higher cell densities and better resistance to radiation doses.

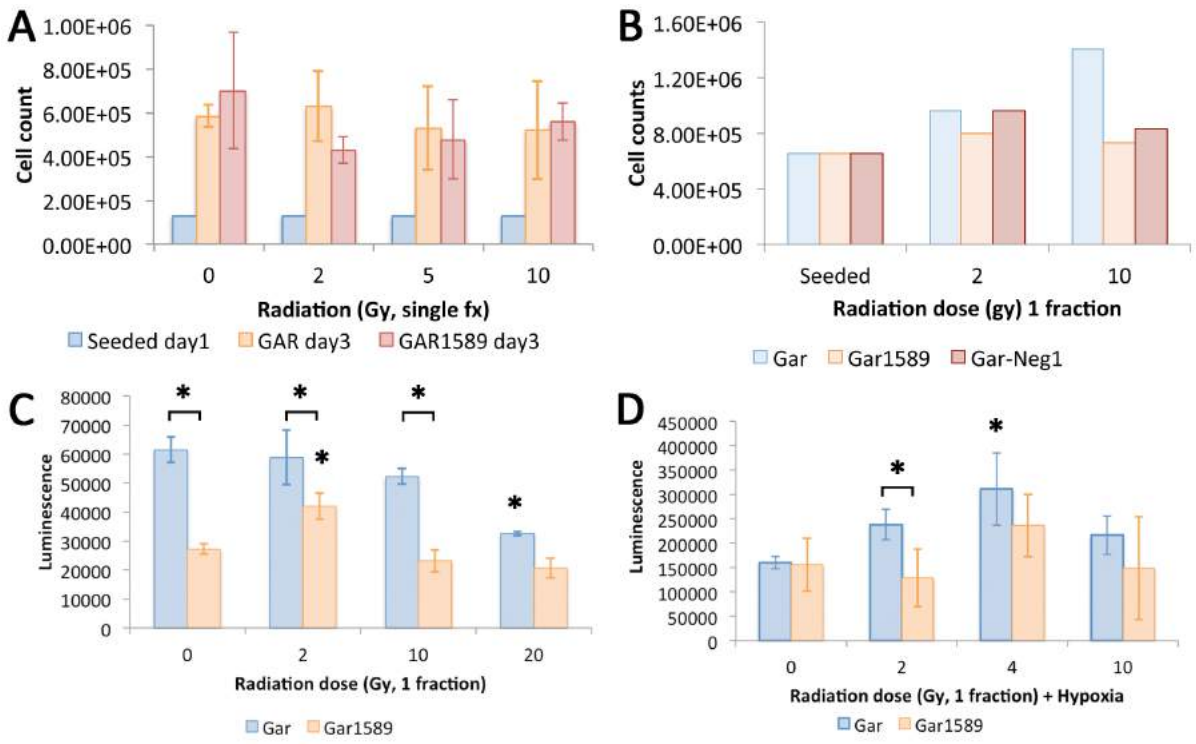

FIGURE 3.4: Impact of *HIF1A* knockout, high-dose radiation, and hypoxia in GAR meningioma cell lines

A) Preliminary analysis of cell counts after 2-, 5-, or 10-Gy single-fraction radiation doses suggested did not show a significant difference in GAR (p=0.99, one-way ANOVA) or GAR1589 cells (p=0.40, one-way ANOVA). B) Cell counts with inclusion of GAR-NEG cells, cells with scrambled RNA, were compared to GAR1589 cells. C) Single-radiation fractions in normoxic conditions showed a significant difference between GAR and GAR1589 for control (p=0.0001, T-test), 2 Gy (p=0.05), and 10 Gy (p=0.02) treatments, but no difference at 20-Gy (p=0.07) treatments. Evaluation of GAR cells showed a difference only between control and 20 Gy (p=0.028, one-way ANOVA; post-hoc control vs. 20 Gy, p=0.024). GAR1589 cells showed a significant increase in viability after 2-Gy treatment (p=0.008, one-way ANOVA; post-hoc control vs. 2Gy, p=0.024). D) Hypoxic treatment conditions generally reduced the difference between GAR and GAR1589 after treatment. A significant difference between GAR and GAR1589 cells was seen at 2 Gy (p=0.05, T-test) but not control (p=0.9), 4 Gy (p=0.3) or 10 Gy (p=0.4). An increase in viability at 4 Gy was seen for GAR cells (p=0.022, one-way ANOVA; post-hoc control vs. 4Gy, p=0.015). No difference between treatment conditions for GAR1589 was seen (p=0.361).

FIGURE 3.5: Impact of *HIF1A* knockout, fractionated radiation, and hypoxia in GAR and GAR1589 meningioma cell lines

A) Cell growth curves in normoxic environments were evaluated. A significant increase in cell count was seen for GAR cells at 4 and 5 days (p=0.0001, one-way ANOVA; control vs. day 4, p=0.006; control vs. day 5, p=0.0001). Similarly, an increase in cell count was seen for GAR1589 cells at 3, 4, and 5 days (p=0.0001, one-way ANOVA; control vs. day 3, p=0.035; control vs. day 4, p=0.09; control vs. day 5, p=0.0001). No difference in GAR-NEG (p=0.081) or GAR1589 cells was seen over time with 2-Gy daily fractions (one-way ANOVA). B) A ratio of cell counts compared to baseline is shown for GAR-NEG and GAR1589 cells in normoxic conditions after radiation treatment. C) Evaluation of cell counts in hypoxic environments was performed. GAR cells showed a significant increase in cell count at 3 days (p=0.03, one-way ANOVA); however cell counts of GAR1589 cells (p=0.075), GAR-NEG cells with hypoxia and radiation (p=0.75), and GAR1589 cells with hypoxia and radiation (p=0.06) did not change over time. D) A ratio of cell counts compared to baseline is shown for GAR-NEG and GAR1589 cells in hypoxic conditions after radiation treatment. E) Cell viability assays in normoxic conditions showed a significant decrease in viability for GAR1589 cells at control (p=0.01, T-test). No difference was seen at 1 (p=0.21) and 2 (p=0.15) days of radiation while a significant decrease in GAR1589 viability was seen at day 3 (p=0.01). GAR1589 cells also showed a decrease in viability at 3 days of treatment compared with day 1 (p=0.007, one-way ANOVA; day 1 vs. day 3, p=0.019). GAR cells did not show a difference in viability over time (p=0.26). F) During hypoxia, there was no difference in cell viability for GAR (p=0.18, one-way ANOVA) or GAR1589 (p=0.097) over time.

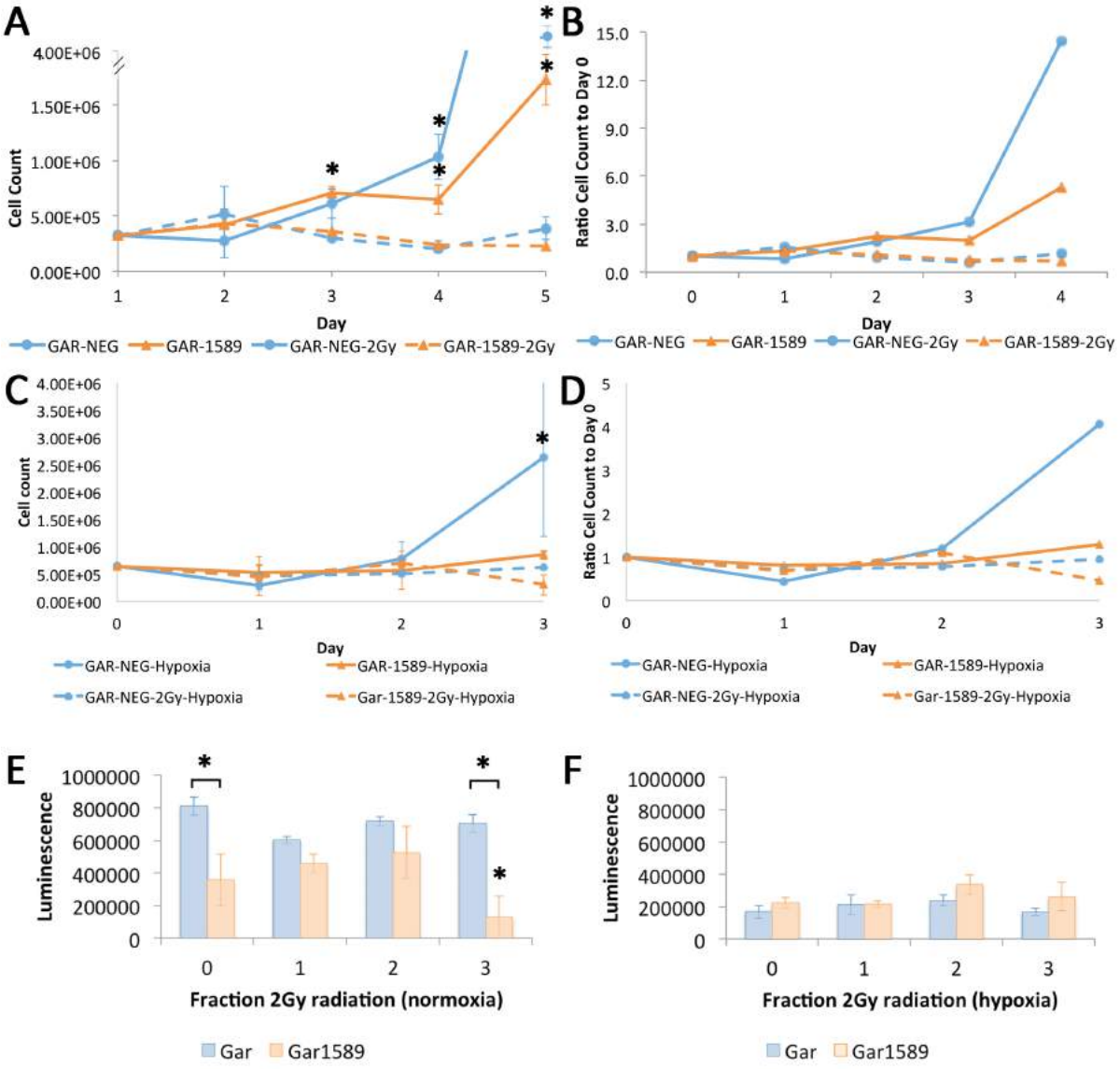
A
Cell Count
4.00E+06
1.50E+06
1.00E+06
5.00E+05
0.00E+00
1
2
3
4
5
Day
GAR-NEG
GAR-1589
GAR-NEG-2Gy
GAR-1589-2Gy
B
Ratio Cell Count to Day 0
15.0
12.0
9.0
6.0
3.0
0.0
0
1
2
3
4
Day
GAR-NEG
GAR-1589
GAR-NEG-2Gy
GAR-1589-2Gy
C
Cell count
4.00E+06
3.50E+06
3.00E+06
2.50E+06
2.00E+06
1.50E+06
1.00E+06
5.00E+05
0.00E+00
0
1
2
3
Day
GAR-NEG-Hypoxia
GAR-1589-Hypoxia
GAR-NEG-2Gy-Hypoxia
Gar-1589-2Gy-Hypoxia
D
Ratio Cell Count to Day 0
5
4
3
2
1
0
0
1
2
3
Day
GAR-NEG-Hypoxia
GAR-1589-Hypoxia
GAR-NEG-2Gy-Hypoxia
Gar-1589-2Gy-Hypoxia
E
Luminescence
1000000
800000
600000
400000
200000
0
0
1
2
3
Fraction 2Gy radiation (normoxia)
Gar
Gar1589
F
Luminescence
1000000
800000
600000
400000
200000
0
0
1
2
3
Fraction 2Gy radiation (hypoxia)
Gar
Gar1589

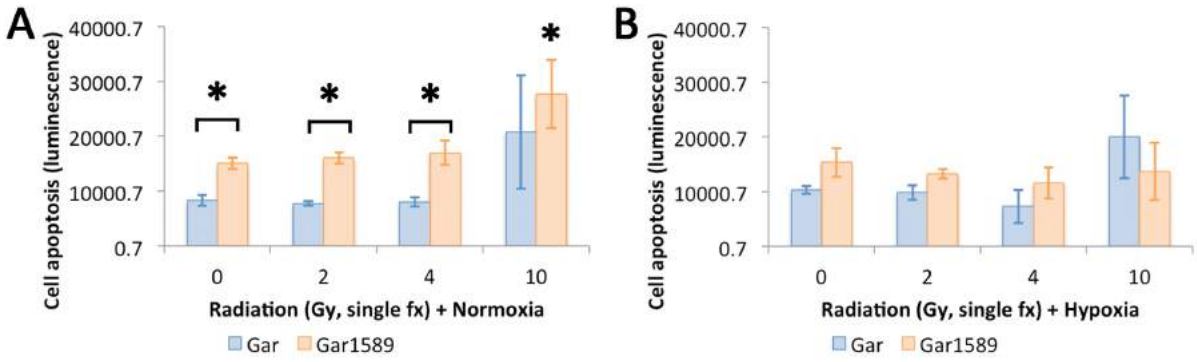

FIGURE 3.6: Impact of *HIF1A* knockout and radiation on apoptosis in meningioma

Apoptosis was evaluated to identify potential mechanisms of *HIF1A* knockout, radiation, and hypoxia. A) Cell apoptosis in normoxia significantly increased at control (p=0.001, t-test), 2 Gy (p=0.001) and 4 Gy (p=0.01) but not 10 Gy (p=0.31). Apoptosis significantly increased with higher doses in GAR1589 cells (p=0.04, one-way ANOVA; control and 10 Gy, p=0.008). B) Hypoxic conditions reduced the difference between cell lines. No difference in apoptosis between cell lines was seen for control (p=0.07, t-test), 2 Gy (p=0.06), 4 Gy (p=0.15), or 10 Gy (p=0.31) treatments. Comparison of cell lines across treatments showed no difference for GAR (p=0.024, one-way ANOVA; no significant post-hoc comparison) or GAR1589 cells (p=0.59).

FIGURE 3.7: Impact of *HIF1A* mutation on live cell proliferation

Evaluation of cell confluency and correlation with cell proliferation was performed. A) GAR cells were grown and received 10Gy or 20Gy of radiation in a single fraction. Cells slowed proliferation after treatment and demonstrated a linear growth pattern that plateaued at a lower confluency than control cells. B) GAR1589 cells received radiation and showed greater susceptibility to treatment. C) GAR and GAR1589 cells are shown together after 10 or 20Gy single fraction treatments. D) A ratio of GAR and GAR1589 cells compared to baseline demonstrates similar effects for radiation in all cells up to approximately 100 days followed by changes in proliferative capacity thereafter. E) Photomicrographs with automated confluency maps are shown for cell lines and treatment conditions with corresponding video snapshots.

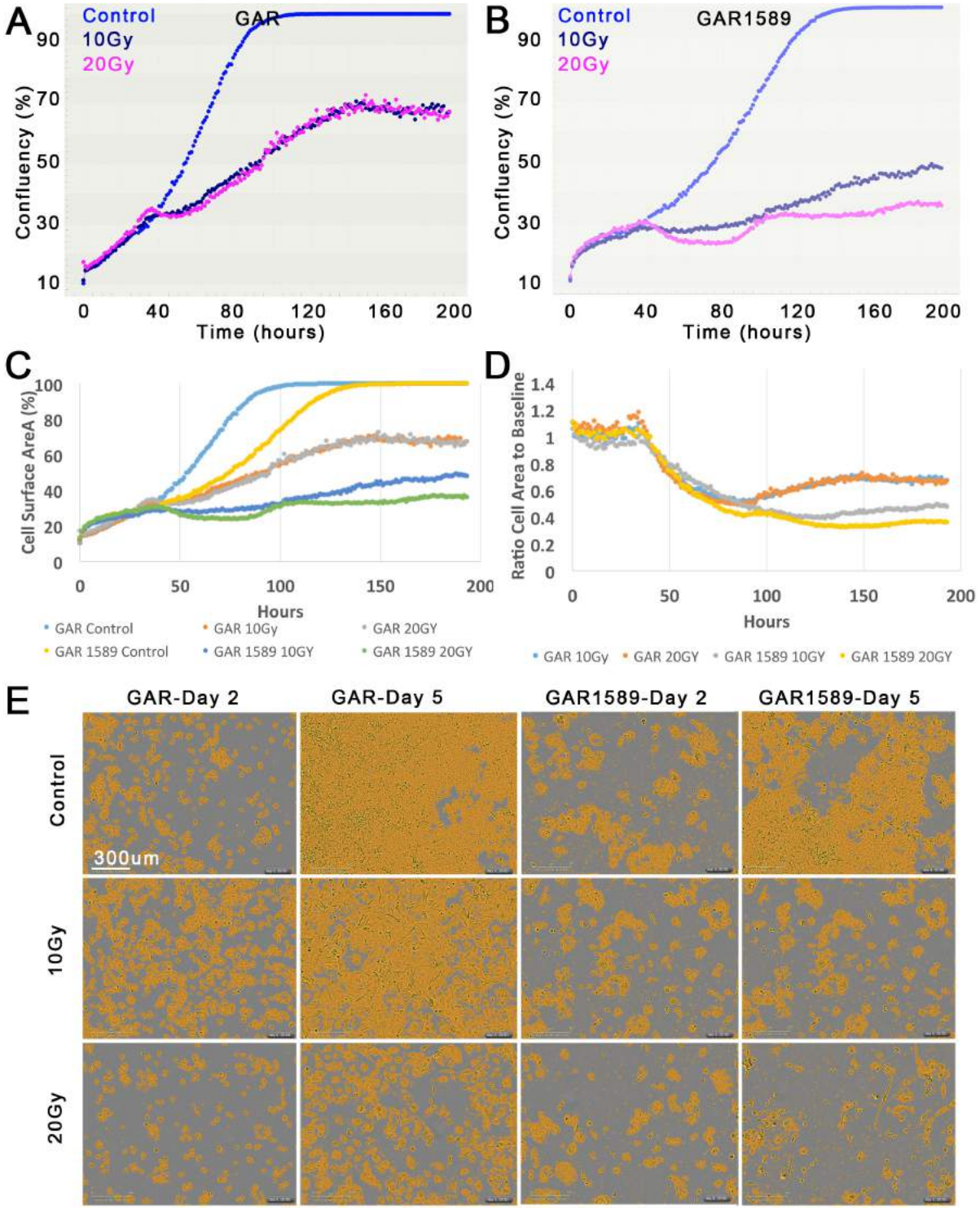
A
Control
10Gy
20Gy
GAR
Confluency (%)
Time (hours)
B
Control
10Gy
20Gy
GAR1589
Confluency (%)
Time (hours)
C
Cell Surface AreA (%)
Hours
GAR Control
GAR 10Gy
GAR 20GY
GAR 1589 Control
GAR 1589 10GY
GAR 1589 20GY
D
Ratio Cell Area to Baseline
Hours
GAR 10Gy
GAR 20GY
GAR 1589 10GY
GAR 1589 20GY
E
GAR-Day 2
GAR-Day 5
GAR1589-Day 2
GAR1589-Day 5
Control
10Gy
20Gy
300um

FIGURE 3.8: Colony formation assay of meningioma and response to radiation

A) Dark field microscopy demonstrated formation of meningioma neurospheres in a soft agar CFA. GAR cells showed a greater number than GAR1589 cells. Treatment with a single dose of 2Gy and 10Gy radiation showed a decrease in colony count and size. B) Staining of colonies with 0.005% crystal violet demonstrated higher colony counts with GAR cells compared to GAR1589 cells. Treatment with radiation reduced colony number. C) Quantification of % total area for dark field microscopy showed a decrease in area after radiation treatments, which was not statistically different ($p=0.12$, one-way ANOVA). D) After crystal violet staining, % total area of colonies was significantly reduced ($p=0.0001$) for GAR cells at 2Gy ($p=0.001$) and 10Gy ($p=0.0001$), as well as GAR1589 ($p=0.0001$) at 2Gy ($p=0.0001$) and 10Gy ($p=0.0001$). E) Colony count was also after radiation ($p=0.0001$) for GAR cells at 2Gy ($p=0.007$) and 10Gy ($p=0.011$) as well as GAR1589 ($p=0.0001$) at 2Gy ($p=0.003$) but not 10Gy ($p=0.074$). *$p<0.05$, one-way ANOVA with Tukey post-hoc comparison.

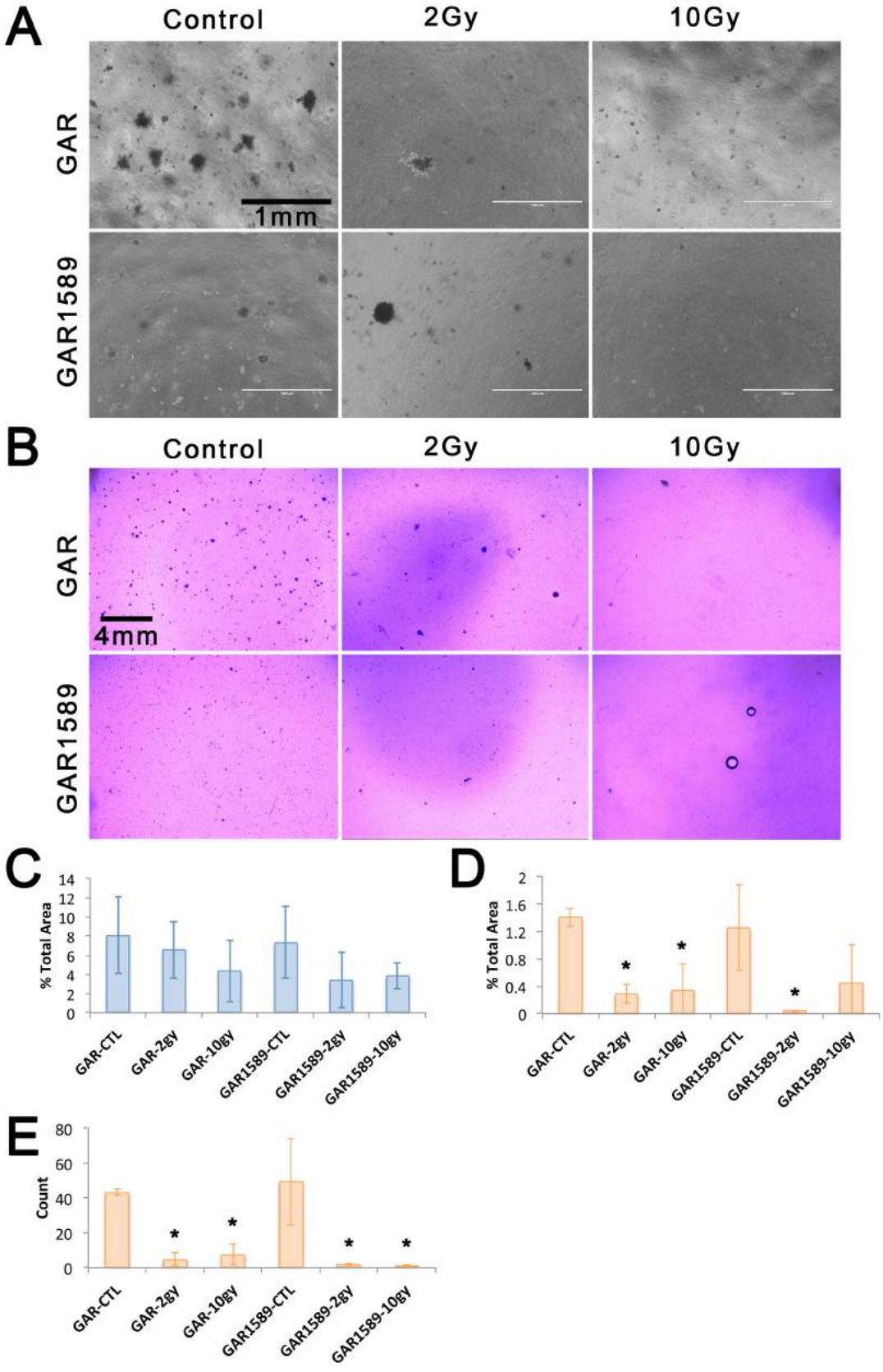
A
Control
2Gy
10Gy
GAR
GAR1589
1mm
B
Control
2Gy
10Gy
GAR
GAR1589
4mm
C
% Total Area
0
2
4
6
8
10
12
14
GAR-CTL
GAR-2gy
GAR-10gy
GAR1589-CTL
GAR1589-2gy
GAR1589-10gy
D
% Total Area
0
0.4
0.8
1.2
1.6
2
*
*
*
GAR-CTL
GAR-2gy
GAR-10gy
GAR1589-CTL
GAR1589-2gy
GAR1589-10gy
E
Count
0
20
40
60
80
*
*
*
*
GAR-CTL
GAR-2gy
GAR-10gy
GAR1589-CTL
GAR1589-2gy
GAR1589-10gy

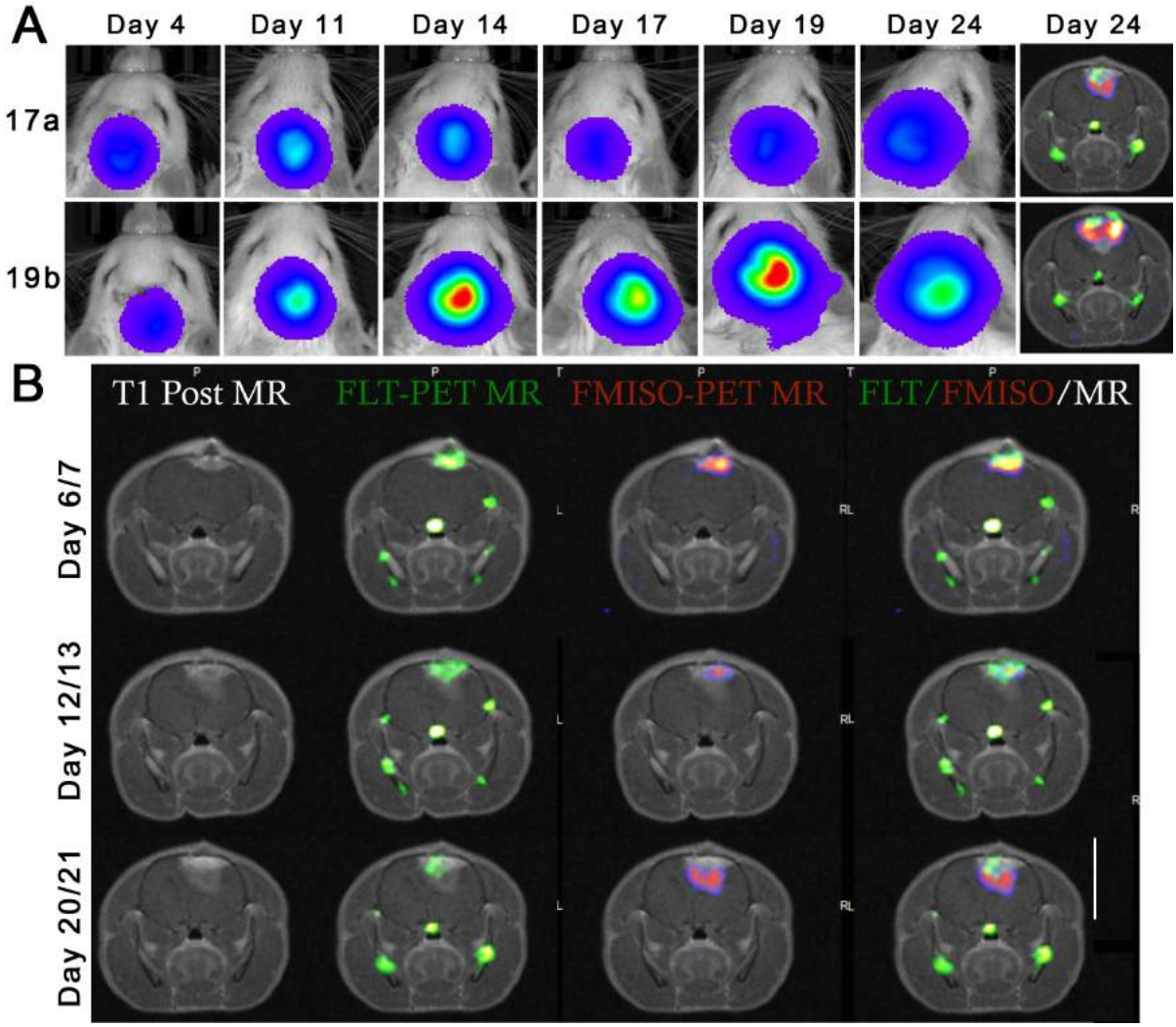

FIGURE 3.9: Luciferase, MRI, and PET imaging after tumor injection is demonstrated

A) Luciferase imaging over time shows expansion of the cell line injected in the right frontal lobe. Variation in cell proliferation rates and total expression are seen. MRI/PET imaging at day 24 is shown for each animal (FMISO [red], FLT [green]). B) Similarly, FMISO (red) and FLT (green) PET MRI are shown at 3 different time points. MRI involves a contrast-enhancing T1 sequence. FMISO expression tails FLT as expected since hypoxic areas follow tumor proliferation.

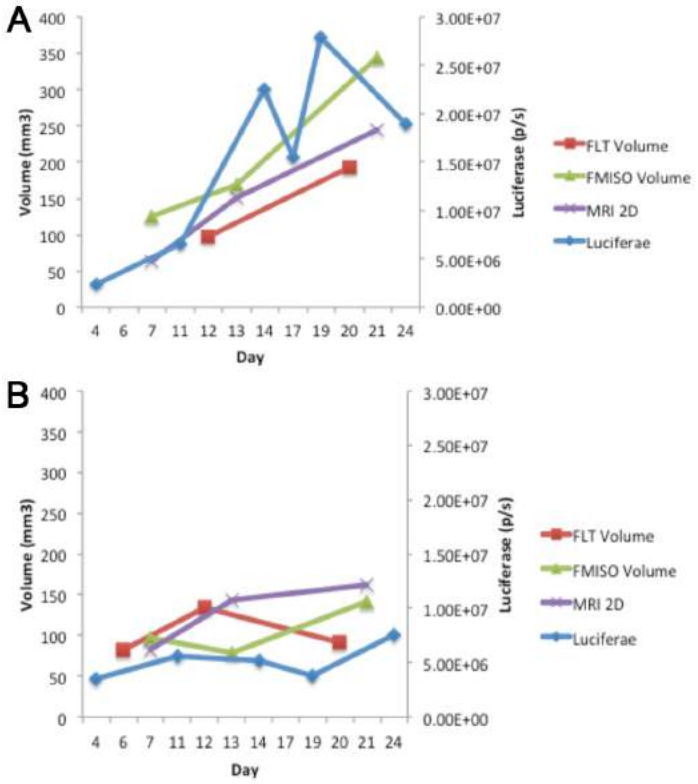

FIGURE 3.10: Quantified MRI, PET, and luciferase imaging of hypoxia

A,B) Quantification of two distinct animals (17a and 19b) animals from Figure 3.9 are shown over time for FLT volume, FMISO volume, MRI volume, and luciferase expression.

CHAPTER 4

DISCUSSION

4.1 Clinical correlation of microvascular density in meningiomas

Tumor microvascularity plays an important role in tumor biology, patient prognosis, and treatment development. Our study show that various clinical and microvascularity measures in meningioma patients could be predictive of tumor size, EBL, PFS, and OS. Tumors ≥3 cm showed significantly greater staining for MIB and vWF as well as lower HIF-1 expression compared with tumors <3 cm. Moreover, a significantly worse OS was seen with larger tumors, which showed an average of 19 months shorter survival. The vWF microvascularity measure predicted EBL, showing greater expression in tumors with greater EBL despite tumor size. These results suggest that assessment of vWF may be able to detect an alteration in tumor biology with larger meningiomas. Multivariate analysis showed that CD105 and possibly MIB predicted OS, but only MIB showed a trend on a hazard model and was thus further evaluated. Survival analysis showed that a MIB index ≥3 demonstrated high specificity (82.5%) but not sensitivity (36%) for predicting PFS, suggesting that elevated MIB could be useful in predicting tumor recurrence regardless of size or other factors. However, tumors with low MIB could not be ruled out from possible future progression. The ease of calculation of MIB adds to its potential value as a practical clinical tool. These results suggest a

potential benefit from the inclusion of microvascularity measurements in the prediction of morbidity and mortality from grade I meningioma and provide a greater understanding of underlying tumor biology.

4.2 Utility of microvascularity measures in meningiomas

Microvascularity measures were useful in predicting tumor size, EBL, and PFS. Of the various factors evaluated, MIB, vWF and HIF-1 were most predictive of tumor size, vWF of EBL, and MIB of PFS. Various microvascularity measurements have been described in the literature as having diverse effects depending on tumor type and grade. CD105 has been reported to be a more specific marker of neovascularization in meningiomas by staining newly formed vessels but not pre-existing ones (84). Expression of CD105 has been shown to correlate with shorter PFS in patients with Simpson grade 1 resections (57). CD34 was reported as a more sensitive marker of meningioma compared with CD31 (85).

A better understanding of tumor microvasculature in meningiomas may help us improve targeted therapies as well as understanding regarding resistance to anti-angiogenic molecules. Tumor vessels in meningioma, as well as other tumors, demonstrate multiple distinct abnormalities from normal vessels including abnormal capillary division, glomeruloid bodies, and abnormal molecular signaling, such as within VEGF and HIF-1 (48, 59); however, not all studies have shown a correlation between VEGF expression, microvascularity, and meningioma WHO grade (86). Although anti-VEGF inhibitors, namely bevacizumab, have been evaluated in meningioma, results demonstrating a sustained tumor response remain limited (9). It is likely that multiple signaling pathways are involved in regulating angiogenesis in meningiomas and that

single markers may not be sufficient to categorize these findings. The strong correlation among the various microvascularity measurements in our study suggest that identifying one robust marker could be sufficient to predict other changes in angiogenesis, but further study of the key angiogenic pathways is warranted.

Our results are also the first to explore the use of fractal-based microvascular assessment in grade I meningiomas, and we were able to quantify the complexity of the microvascular patterns in an automated fashion. Automated microvascular assessment has been a useful tool in evaluating a variety of tumors, including malignant tumors (59, 60) and pituitary tumors (55). Our results failed to show a significant correlation of fractal-based microvascular assessment with either PFS or OS. It is likely that markers vary on their sensitivity and specificity of assessing tumor vascularity (55-57). While these fractal-based markers have been more successful for aggressive tumors, they may have been more limited for grade I meningiomas in our series because differences in microvascularity may have been subtler. Further study is required to evaluate fractal-based microvascular measurements in meningiomas and other neurological tumors.

4.3 Practical MIB thresholds for clinical use

MIB index can be a useful tool in evaluating meningioma aggressiveness. While MIB-1 has correlated with outcomes in some studies (87-98), this correlation has not been seen in other studies (99-103). Various cutoffs for MIB in predicting disease grade and progression have been suggested, including 15% (98), 4.2% (96), 3% (58, 87, 89, 94), 2.6% (97), and 2% (93). Our results suggest a value of 3% shows 82.5% specificity in predicting disease progression but only 36% sensitivity. In other words, patients with MIB indices ≥3% showed a high likelihood of tumor progression, but patients with MIB

indices <3% could not necessarily be ruled out from future disease progression. In a meta-analysis of 53 studies, average cutoffs for grade I, II, and III meningiomas were 3%, 8%, and 17%, respectively (104). A recent study of 240 patients with grade I meningioma from a single center showed that among patients who had Simpson Grade II and III resections, an MIB-1 index of ≥3% was predictive of shorter time to recurrence (95). The effect of MIB-1 in this study was also seen in a Cox proportional hazards model (OR 4.65, 95% CI 1.59, 14.0; p=0.006). These results are reflective of our findings showing MIB to be a significant predictor of progression, although a lower OR of 1.14 was found in our series. Our previous results support good intra- and inter-observer reliability between MIB measurements (81). Nevertheless, not all areas of a tumor are typically evaluated during pathological evaluation, which may account for the variation in MIB thresholds among different studies.

4.4 Noninvasive methods of microvascularity assessment

Recent studies have supported various imaging modalities to quantify tumor vascularity to better target treatment and predict prognosis. Perfusion MRI is one modality that allows for quantitation of vascularity parameters by compartmental modeling and has been shown to predict outcome in gliomas (22, 105) and meningiomas (106). Imaging markers of vascularity have been shown to correlate with and predict MIB index (107) and VEGF expression(108) during immunohistological analysis of meningiomas in some studies, although other studies have not shown correlation between imaging and pathological markers (109). Assessment of vascularity has also been suggested to aid in distinguishing tumor progression from pseudoprogression or radiation necrosis (16). These imaging modalities may serve as useful adjuvant tools for clinicians

to assess the aggressiveness of a tumor prior to resection and guide surgical treatment and also as a method of noninvasive evaluation of tumors on follow-up.

Preoperative noninvasive measures of microvascularity can also be helpful in improving surgical strategies to reduce patient morbidity. In addition, the limited response of central nervous system tumors to anti-angiogenic treatments in meningiomas and other diseases can be evaluated by examining tumor vasculature on dynamic MRI (110). One hypothesis has been that anti-angiogenic therapies may result in transient normalization of tumor vasculature as opposed to destruction of tumor vessels (111). Tumor responsiveness to radiotherapy also greatly depends on vascularity, and evaluation of microvascularity may be a useful strategy of selecting patients for adjuvant therapies.

4.5 Limitations of microvascularity measurements in meningiomas

Our results did not include Simpson grade or evaluate the use of postoperative radiotherapy. Although most patients with grade I meningiomas in our series underwent a Simpson grade I resection, intraoperative and postoperative imaging were not evaluated in a blinded manner. Several recent studies have suggested limits on the usefulness of Simpson grading to predict recurrence (6, 95), although short follow-up has been one limitation of these data. Our results suggested that MIB-1 could help explain meningioma recurrence after subtotal resection and be a useful adjuvant to Simpson grading. In addition, the impact of adjuvant radiotherapy on tumor recurrence was not delineated. Our study also omitted grade II and III meningiomas, which may have been helpful in evaluating the various markers of microvascularity evaluated in this study. Localization of removed tissue to specific areas of a tumor (e.g., hypoxic core, subcapsular penumbra) and analysis of microvascular density could improve understanding of measurements.

4.6 Summary of microvascularity measurements in meningiomas

Our results support the assertion that evaluation of microvascularity has a role in differentiation of tumor volume, EBL, PFS, and OS in patients with grade I meningioma. Specific measures of microvascularity were predictive of preoperative (e.g., MIB, vWF and HIF-1 for tumor size), intraoperative (e.g., vWF in EBL), and postoperative (e.g., MIB for PFS) outcomes in patients with grade I meningiomas. No specific factor was robust in determining OS; however, an MIB index cutoff of 3 showed a specificity of 86.5% and sensitivity of 36% in predicting PFS, suggesting it could be used to identify patients likely to progress only when positive. Microvascularity likely plays an important role in the disease progression of grade I meningiomas and has the potential to aid in the prediction of patient morbidity and mortality.

4.7 Radioresistance in meningiomas

Several findings regarding radiation resistance in meningiomas were explored in this study. Increased cell density played a role in reducing response to radiation while at lower cell densities, increased proliferation of primary meningioma cells was seen. The results of this study suggest that HIF1 plays a role in the radioresistance of meningioma. After knockdown of HIF1 expression, GAR-1589 meningioma cells showed a slower proliferation rate compare to their wild-type GAR counterparts. Single fractions of radiation decreased proliferation of GAR-1589 cells at all doses compared to GAR cells; the difference between cells was eliminated in hypoxic environments. Fractionated doses of radiation could suppress meningioma cell growth more effectively in GAR-1589 cells. However neither cell line was completely eliminated. Apoptosis was significantly increased after HIF1 knockdown and radiation treatments. Continuous monitoring of

cells showed that single fractions were able to suppress cell proliferation kinetics, cells were unable to reach a confluency plateau, and GAR-1589 cells showed slower growth rates. Culturing in 3D showed diminished colony formation in GAR and GAR-1589 cells with both low and high dose radiation treatments, a distinct effect from cells in 2D culture environments. These results suggest HIF1 plays a role on radiation resistance in meningiomas depending on cell density, radiation fractions and dose, as well as *in vitro* culture conditions.

4.8 Clinical use of radiotherapy in meningiomas

Currently, radiation therapy plays a key role in benign and malignant meningioma. Benign lesions <3 cm in maximal diameter can be treated with stereotactic radiosurgery, involving a single high dose of conformed ionizing radiation, with subsequent close follow-up. Several meta-analyses report tumor control rates of 85–100% for benign meningiomas (112, 113). In addition, a meta-analysis evaluating radiation for atypical or anaplastic meningiomas showed median overall 5-year survival rates of 67.5% and 55.6%, respectively (114). Radiotherapy did result in improved local control of atypical or anaplastic meningiomas after subtotal resection. Our results suggest that cell density may be a factor in larger meningiomas and more aggressive meningiomas. Treatments with high doses of single-fraction radiation and fractionated radiotherapy were both effective in suppressing tumor growth. However neither could fully eliminate cells. It may be possible to extrapolate some of the findings of this study towards clinical patients, namely the utility of high-dose radiation and adequate oxygen environment for meningiomas, but further animal and clinical experiments will be necessary to confirm these findings.

4.9 Molecular mechanisms of radiotherapy in meningiomas

Among the important molecules involved in radiation efficacy for meningiomas, urokinase receptor (uPAR) has been shown to be important in response to radiation (115-117). uPAR is a membrane-bound glycoprotein with roles in wound healing, proteolysis, and nonproteolytic processes, such as cell migration, cell cycle regulation, and cell adhesion. Loss of uPAR resulted in increased apoptosis with radiation and decreased cell migration as well as combined synergistically with radiation to inhibit cell proliferation (115, 116, 118). Within meningiomas, uPAR has also been shown to play a role in angiogenesis (119), to induce upregulation of activated *MAPK*, *nuclear factor κB* (*NF-kB*) *p51*, and *monocyte chemoattractive protein-1* (*MCP-1*) (120), and to induce apoptosis by inactivating p53 translocation (121). Other molecular mechanisms implicated in radiotherapy include increased expression of alpha3 and beta1 integrins with radiation (118), increased radiation sensitivity with low expression of *p16*, *CDK6*, and *pRb* (122), and defective response to ultraviolet and gamma irradiation with p53/p21 loss (123). Genomic studies have also identified meningioma-specific genes associated with WHO grades and the ability to classify tumors (124). Genes that are differentially expressed in meningioma after radiotherapy have yet to be explored and could be evaluated by gene expression arrays.

4.10 Impact of *HIF1A* on radiation responsiveness

The important role for radiation and HIF1A in tumors has been demonstrated (125). A seminal study by Moeller et al. (126) showed increased expression of HIF1A after fractionated radiotherapy in xenografted adenocarcinoma tumors with a delay of 12–24 hours after radiation. In addition, downstream proteins from the HIF1A signaling

pathway, such as VEGF, fibroblast growth factor (bFGF), and plasminogen activator inhibitor-1 (PAI-1), were upregulated. Moreover, radiation treatment induced HIF1A expression even in the setting of hypoxia, as assessed by pimonidazole staining, and HIF1A effects depended on reactive oxygen species production. Finally, tumor-induced vascularization depended on oxygen status and HIF1A. HIF1A has been shown to affect apoptosis through upregulation of proapoptotic BINP3 (127) and stabilization of p53 (128). The radiosensitizing effect induced by HIF1A on tumor vasculature is pronounced (129). HIF1A promotes ATP metabolism, cell proliferation, and p53 activation.

4.11 Limitations of *HIF1A* analysis in meningiomas

Several limitation of this *in vitro* work were identified. Limited HIF1 levels (~15-20% suppression) were identified in GAR-1589 cells compared to parent GAR cells likely due to the difficulty in infecting primary meningioma cells with shRNA plasmid. This may have resulted in GAR and GAR-1589 cells showing similarities in cell proliferation, and response to hypoxia. The use of a CRISPR/Cas9 knockout of HIF1A in meningioma cells may be a more effective method to compare the effects of HIF1A knockout. The additional use of drugs that inhibit HIF1 (e.g., YC-1, chetomin, chrysin) or stabilize HIF1 (e.g., dimethyloxaloylglycine, desferrioxamine) could be additional methods to elucidate HIF1-signaling. Use of expression microarray profiles can also help evaluate HIF1 involved pathways. However our results suggest that cell culture and radiation treatment conditions would play a large role in potentially affecting gene expression patterns.

4.12 Summary of *HIF1A* and radiotherapy in meningiomas

The results of this study provide evidence for the importance of three factors that affect meningioma response to radiation—cell density, dependence on HIF1A mutation of radiation sensitivity, and oxygen tension. These results add to the current molecular understanding of meningioma and its response to radiation. The results of this study support the importance of HIF1A and hypoxia in regulating sensitivity to radiation in meningiomas. Our results suggested that HIF1A loss could be beneficial with concurrently applied radiotherapy. Future directions can involve combined radiotherapy and targeting of HIF1A or is subsequent pathway.

4.13 Proof-of-principle multimodal rodent imaging models

The results of multimodal imaging suggest that syngenic, orthotopic animal model can be helpful for *in vivo* modeling of tumor growth and behavior characteristics. Our results suggest that imaging of hypoxia (e.g., FMISO) and proliferation (e.g., bioluminescence, FLT) can be performed for tumor models allowing for study of tumors in the native microenvironment. Tumor proliferation preceded tumor hypoxia and localization of centralized hypoxic signaling could be seen in a glioma cell model. Previous studies suggest that orthotopic models can better approximate the clinical environment, where the blood-brain barrier plays a role in drug penetration (10). Multimodal imaging via bioluminescence, PET tracers and MRI are useful in evaluating various features of tumor pathogenesis (70-72). Imaging of perfusion can improve tissue biopsies, prediction of tumor recurrence, and assessment of treatment response. In addition, evaluation of location specific hypoxia can be performed noninvasively using multimodal imaging. Future work will involve the use of *HIF1A* knockout meningioma

cell lines in comparison to wild-type cells, as well as evaluation of radiation responsiveness and tumor growth behavior.

CHAPTER 5

CONCLUSION

Key findings of this study focus on importance of microvascularity measurements clinically, the impact of HIF1A on radiation, as well as the development of several new cell lines (e.g., GAR-CRISPR-HIF1A), tools (e.g., *in vitro* cell culture and *in vivo* rodent brain radiation shielding) and techniques (e.g., multimodal bioluminescence, PET and MR imaging) for assessing tumor proliferation both *in vitro* and *in vivo*. Future studies include the further characterization of the GAR-CRISPR-HIF1A cell line and development of additional HIF1A knockout cell lines, screening of radiosensitizing treatments in meningiomas, and further characterization of multimodal imaging techniques.

The ultimate goal of this research in better understanding HIF1 signaling is to improve detection, prognosis, and treatment of meningiomas. Development of hypoxia imaging can be clinically useful but has only been used on a research basis. Currently, we have developed a clinical trial protocol involving multimodal MR perfusion, and spectroscopy of both low- and high-grade glial tumors with directed surgical biopsy of tumor locations. Correlation of tumor location with immunohistochemical measurements of microvascularity and HIF1A signaling pathways can improve understanding of tumor biology. In addition, tumor-signaling changes seen on MRI, which can often be unclear

clinically, will be evaluated microscopically.

The results from this study can continue to be hypothesis generating for future studies on meningiomas and other primary brain tumors. Knowledge from this work could be impactful in future patient care. However, only via an improved diagnostic test, treatment protocol, or clinical device can this knowledge truly be applied.

REFERENCES

1. Cushing H (1922) The meningiomas (dural endotheliomas): Their source and favoured seats of origin. *Brain* 45:282-316.

2. Louis DN*, et al.* (2016) The 2016 World Health Organization classification of tumors of the central nervous system: A summary. *Acta Neuropathol* 131(6):803-820.

3. Ostrom QT*, et al.* (2015) CBTRUS statistical report: Primary brain and central nervous system tumors diagnosed in the United States in 2008-2012. *Neuro Oncol* 17 Suppl 4:iv1-iv62.

4. Longstreth WT, Jr., Dennis LK, McGuire VM, Drangsholt MT, & Koepsell TD (1993) Epidemiology of intracranial meningioma. *Cancer* 72(3):639-648.

5. Sughrue ME*, et al.* (2010) Treatment decision making based on the published natural history and growth rate of small meningiomas. *J Neurosurg* 113(5):1036-1042.

6. Sughrue ME*, et al.* (2010) The relevance of Simpson Grade I and II resection in modern neurosurgical treatment of World Health Organization Grade I meningiomas. *J Neurosurg* 113(5):1029-1035.

7. Rogers L*, et al.* (2015) Meningiomas: Knowledge base, treatment outcomes, and uncertainties. A RANO review. *J Neurosurg* 122(1):4-23.

8. Riemenschneider MJ, Perry A, & Reifenberger G (2006) Histological classification and molecular genetics of meningiomas. *Lancet Neurol* 5(12):1045-1054.

9. Karsy M, Guan J, Cohen A, Colman H, & Jensen RL (2016) Medical management of meningiomas: Current status, failed treatments, and promising horizons. *Neurosurg Clin N Am* 27(2):249-260.

10. Karsy M*, et al.* (2016) Combined hydroxyurea and verapamil in the clinical treatment of refractory meningioma: Human and orthotopic xenograft studies. *World Neurosurg* 86:210-219.

11. Pham MH*, et al.* (2011) Molecular genetics of meningiomas: A systematic review

of the current literature and potential basis for future treatment paradigms. *Neurosurg Focus* 30(5):E7.

12. Clark VE*, et al.* (2013) Genomic analysis of non-NF2 meningiomas reveals mutations in TRAF7, KLF4, AKT1, and SMO. *Science* 339(6123):1077-1080.

13. Clark VE*, et al.* (2016) Recurrent somatic mutations in POLR2A define a distinct subset of meningiomas. *Nat Genet* 48(10):1253-1259.

14. Gillespie DL*, et al.* (2009) Silencing of HIF-1alpha by RNA interference in human glioma cells in vitro and in vivo. *Methods Mol Biol* 487:283-301.

15. Jensen R & Lee J (2012) Predicting outcomes of patients with intracranial meningiomas using molecular markers of hypoxia, vascularity, and proliferation. *Neurosurgery* 71(1):146-156.

16. Jensen RL (2006) Hypoxia in the tumorigenesis of gliomas and as a potential target for therapeutic measures. *Neurosurg Focus* 20(4):E24.

17. Womeldorff M, Gillespie D, & Jensen RL (2014) Hypoxia-inducible factor-1 and associated upstream and downstream proteins in the pathophysiology and management of glioblastoma. *Neurosurg Focus* 37(6):E8.

18. Bar EE, Lin A, Mahairaki V, Matsui W, & Eberhart CG (2010) Hypoxia increases the expression of stem-cell markers and promotes clonogenicity in glioblastoma neurospheres. *Am J Pathol* 177(3):1491-1502.

19. Ando H*, et al.* (2013) A hypoxia-inducible factor (HIF)-3alpha splicing variant, HIF-3alpha4 impairs angiogenesis in hypervascular malignant meningiomas with epigenetically silenced HIF-3alpha4. *Biochem Biophys Res Commun* 433(1):139-144.

20. Reszec J, Rutkowski R, & Chyczewski L (2013) The expression of hypoxia-inducible factor-1 in primary brain tumors. *Int J Neurosci* 123(9):657-662.

21. Gillespie DL*, et al.* (2007) Silencing of hypoxia inducible factor-1alpha by RNA interference attenuates human glioma cell growth in vivo. *Clin Cancer Res* 13(8):2441-2448.

22. Jensen RL*, et al.* (2014) Preoperative dynamic contrast-enhanced MRI correlates with molecular markers of hypoxia and vascularity in specific areas of intratumoral microenvironment and is predictive of patient outcome. *Neuro Oncol* 16(2):280-291.

23. Rong Y, Durden DL, Van Meir EG, & Brat DJ (2006) 'Pseudopalisading' necrosis in glioblastoma: A familiar morphologic feature that links vascular pathology, hypoxia, and angiogenesis. *J Neuropathol Exp Neurol* 65(6):529-539.

24. Wu Y*, et al.* (2014) Hypoxia inducible factor-1 is involved in growth factor,

glucocorticoid and hypoxia mediated regulation of vascular endothelial growth factor-A in human meningiomas. *J Neurooncol* 119(2):263-273.

25. Karsy M, Guan J, Jensen R, Huang LE, & Colman H (2016) The impact of hypoxia and mesenchymal transition on glioblastoma pathogenesis and cancer stem cells regulation. *World Neurosurg* 88:222-236.

26. Huang LE, Arany Z, Livingston DM, & Bunn HF (1996) Activation of hypoxia-inducible transcription factor depends primarily upon redox-sensitive stabilization of its alpha subunit. *J Biol Chem* 271(50):32253-32259.

27. Goldberg MA, Dunning SP, & Bunn HF (1988) Regulation of the erythropoietin gene: Evidence that the oxygen sensor is a heme protein. *Science* 242(4884):1412-1415.

28. Semenza GL, Nejfelt MK, Chi SM, & Antonarakis SE (1991) Hypoxia-inducible nuclear factors bind to an enhancer element located 3' to the human erythropoietin gene. *Proc Natl Acad Sci U S A* 88(13):5680-5684.

29. Semenza GL (1999) Regulation of mammalian O2 homeostasis by hypoxia-inducible factor 1. *Annu Rev Cell Dev Biol* 15:551-578.

30. Schofield CJ & Ratcliffe PJ (2004) Oxygen sensing by HIF hydroxylases. *Nat Rev Mol Cell Biol* 5(5):343-354.

31. Huang LE & Bunn HF (2003) Hypoxia-inducible factor and its biomedical relevance. *J Biol Chem* 278(22):19575-19578.

32. Huang LE, Gu J, Schau M, & Bunn HF (1998) Regulation of hypoxia-inducible factor 1alpha is mediated by an O2-dependent degradation domain via the ubiquitin-proteasome pathway. *Proc Natl Acad Sci U S A* 95(14):7987-7992.

33. Kallio PJ, Pongratz I, Gradin K, McGuire J, & Poellinger L (1997) Activation of hypoxia-inducible factor 1alpha: Posttranscriptional regulation and conformational change by recruitment of the Arnt transcription factor. *Proc Natl Acad Sci U S A* 94(11):5667-5672.

34. Haddad NM, Cavallerano JD, & Silva PS (2013) Von Hippel-Lindau disease: A genetic and clinical review. *Semin Ophthalmol* 28(5-6):377-386.

35. Mabjeesh NJ & Amir S (2007) Hypoxia-inducible factor (HIF) in human tumorigenesis. *Histol Histopathol* 22(5):559-572.

36. Li Z*, et al.* (2009) Hypoxia-inducible factors regulate tumorigenic capacity of glioma stem cells. *Cancer Cell* 15(6):501-513.

37. Kaelin WG, Jr. & Ratcliffe PJ (2008) Oxygen sensing by metazoans: The central role of the HIF hydroxylase pathway. *Mol Cell* 30(4):393-402.

38. Mahon PC, Hirota K, & Semenza GL (2001) FIH-1: A novel protein that interacts with HIF-1alpha and VHL to mediate repression of HIF-1 transcriptional activity. *Genes Dev* 15(20):2675-2686.

39. Majmundar AJ, Wong WJ, & Simon MC (2010) Hypoxia-inducible factors and the response to hypoxic stress. *Mol Cell* 40(2):294-309.

40. Semenza GL (2010) HIF-1: Upstream and downstream of cancer metabolism. *Curr Opin Genet Dev* 20(1):51-56.

41. Ke Q & Costa M (2006) Hypoxia-inducible factor-1 (HIF-1). *Mol Pharmacol* 70(5):1469-1480.

42. Chi JT*, et al.* (2006) Gene expression programs in response to hypoxia: Cell type specificity and prognostic significance in human cancers. *PLoS Med* 3(3):e47.

43. Semenza GL (2012) Hypoxia-inducible factors: Mediators of cancer progression and targets for cancer therapy. *Trends Pharmacol Sci* 33(4):207-214.

44. Ravi R*, et al.* (2000) Regulation of tumor angiogenesis by p53-induced degradation of hypoxia-inducible factor 1alpha. *Genes Dev* 14(1):34-44.

45. Jiang J, Tang YL, & Liang XH (2011) EMT: A new vision of hypoxia promoting cancer progression. *Cancer Biol Ther* 11(8):714-723.

46. Brem S, Cotran R, & Folkman J (1972) Tumor angiogenesis: A quantitative method for histologic grading. *J Natl Cancer Inst* 48(2):347-356.

47. Bergers G & Hanahan D (2008) Modes of resistance to anti-angiogenic therapy. *Nat Rev Cancer* 8(8):592-603.

48. Ellis LM & Hicklin DJ (2008) VEGF-targeted therapy: Mechanisms of anti-tumour activity. *Nat Rev Cancer* 8(8):579-591.

49. Semenza GL (2016) Dynamic regulation of stem cell specification and maintenance by hypoxia-inducible factors. *Mol Aspects Med* 47-48:15-23.

50. Weidner N, Semple JP, Welch WR, & Folkman J (1991) Tumor angiogenesis and metastasis--correlation in invasive breast carcinoma. *N Engl J Med* 324(1):1-8.

51. Barresi V & Tuccari G (2010) Increased ratio of vascular endothelial growth factor to semaphorin3A is a negative prognostic factor in human meningiomas. *Neuropathology* 30(5):537-546.

52. Guevara P*, et al.* (2010) Angiogenesis and expression of estrogen and progesterone receptors as predictive factors for recurrence of meningioma. *J Neurooncol* 98(3):379-384.

53. Dharmalingam P, Roopesh Kumar VR, & Verma SK (2013) Vascular endothelial

growth factor expression and angiogenesis in various grades and subtypes of meningioma. *Indian J Pathol Microbiol* 56(4):349-354.

54. Pistolesi S*, et al.* (2004) Angiogenesis in intracranial meningiomas: Immunohistochemical and molecular study. *Neuropathol Appl Neurobiol* 30(2):118-125.

55. Di Ieva A*, et al.* (2013) Microvascular morphometrics of the hypophysis and pituitary tumors: From bench to operating theatre. *Microvasc Res* 89:7-14.

56. Chaubal A, Paetau A, Zoltick P, & Miettinen M (1994) CD34 immunoreactivity in nervous system tumors. *Acta Neuropathol* 88(5):454-458.

57. Barresi V, Cerasoli S, Vitarelli E, & Tuccari G (2007) Density of microvessels positive for CD105 (endoglin) is related to prognosis in meningiomas. *Acta Neuropathol* 114(2):147-156.

58. Nico B*, et al.* (2008) Evaluation of microvascular density in tumors: Pro and contra. *Histol Histopathol* 23(5):601-607.

59. Di Ieva A*, et al.* (2012) Computer-assisted and fractal-based morphometric assessment of microvascularity in histological specimens of gliomas. *Sci Rep* 2:429.

60. Di Ieva A (2012) Fractal analysis of microvascular networks in malignant brain tumors. *Clin Neuropathol* 31(5):342-351.

61. Petrirena GJ, Goldman S, & Delattre JY (2011) Advances in PET imaging of brain tumors: A referring physician's perspective. *Curr Opin Oncol* 23(6):617-623.

62. Mendichovszky I & Jackson A (2011) Imaging hypoxia in gliomas. *Br J Radiol* 84 Spec No 2:S145-158.

63. Hyare H, Thust S, & Rees J (2017) Advanced MRI techniques in the monitoring of treatment of gliomas. *Curr Treat Options Neurol* 19(3):11.

64. Masaki Y*, et al.* (2015) The accumulation mechanism of the hypoxia imaging probe "FMISO" by imaging mass spectrometry: Possible involvement of low-molecular metabolites. *Sci Rep* 5:16802.

65. Kobayashi H*, et al.* (2013) Usefulness of FMISO-PET for glioma analysis. *Neurol Med Chir (Tokyo)* 53(11):773-778.

66. Rasey JS*, et al.* (1987) Characterization of radiolabeled fluoromisonidazole as a probe for hypoxic cells. *Radiat Res* 111(2):292-304.

67. Toyonaga T*, et al.* (2016) (18)F-fluoromisonidazole positron emission tomography can predict pathological necrosis of brain tumors. *Eur J Nucl Med*

Mol Imaging 43(8):1469-1476.

68. Hirata K*, et al.* (2012) (1)(8)F-Fluoromisonidazole positron emission tomography may differentiate glioblastoma multiforme from less malignant gliomas. *Eur J Nucl Med Mol Imaging* 39(5):760-770.

69. Hatano T*, et al.* (2013) Biological characteristics of intratumoral [F-18]fluoromisonidazole distribution in a rodent model of glioma. *Int J Oncol* 42(3):823-830.

70. Nedergaard MK*, et al.* (2016) Comparison of (18)F-FET and (18)F-FLT small animal PET for the assessment of anti-VEGF treatment response in an orthotopic model of glioblastoma. *Nucl Med Biol* 43(3):198-205.

71. Fu Y*, et al.* (2016) A Dual Tracer 18F-FCH/18F-FDG PET imaging of an orthotopic brain tumor xenograft model. *PLoS One* 11(2):e0148123.

72. Cher LM*, et al.* (2006) Correlation of hypoxic cell fraction and angiogenesis with glucose metabolic rate in gliomas using 18F-fluoromisonidazole, 18F-FDG PET, and immunohistochemical studies. *J Nucl Med* 47(3):410-418.

73. Gillespie DL*, et al.* (2015) RNA interference targeting hypoxia-inducible factor 1alpha via a novel multifunctional surfactant attenuates glioma growth in an intracranial mouse model. *J Neurosurg* 122(2):331-341.

74. Ramachandran R*, et al.* (2017) Theranostic 3-Dimensional nano brain-implant for prolonged and localized treatment of recurrent glioma. *Sci Rep* 7:43271.

75. Xuesong D*, et al.* (2016) Evaluation of neovascularization patterns in an orthotopic rat glioma model with dynamic contrast-enhanced MRI. *Acta Radiol*:284185116681038.

76. Dhermain FG, Hau P, Lanfermann H, Jacobs AH, & van den Bent MJ (2010) Advanced MRI and PET imaging for assessment of treatment response in patients with gliomas. *Lancet Neurol* 9(9):906-920.

77. Lehmann S*, et al.* (2009) Longitudinal and multimodal in vivo imaging of tumor hypoxia and its downstream molecular events. *Proc Natl Acad Sci U S A* 106(33):14004-14009.

78. Lo Dico A*, et al.* (2014) Validation of an engineered cell model for in vitro and in vivo HIF-1alpha evaluation by different imaging modalities. *Mol Imaging Biol* 16(2):210-223.

79. Ragel BT*, et al.* (2008) A comparison of the cell lines used in meningioma research. *Surg Neurol* 70(3):295-307; discussion 307.

80. McCutcheon IE*, et al.* (2000) Intracranial injection of human meningioma cells in athymic mice: An orthotopic model for meningioma growth. *J Neurosurg*

92(2):306-314.

81. Flynn JR*, et al.* (2008) Hypoxia-regulated protein expression, patient characteristics, and preoperative imaging as predictors of survival in adults with glioblastoma multiforme. *Cancer* 113(5):1032-1042.

82. Kaynar MY*, et al.* (2008) Expression of hypoxia inducible factor-1alpha in tumors of patients with glioblastoma multiforme and transitional meningioma. *J Clin Neurosci* 15(9):1036-1042.

83. Karsy M, Burnett B, Di Ieva A, Cusimano MD, & Jensen RL (2017) Microvascularization of Grade I meningiomas: Effect on tumor volume, blood loss, and patient outcome. *J Neurosurg*:1-10.

84. Barresi V (2011) Angiogenesis as a predictor of recurrence in meningiomas. *J Neurooncol* 101(1):169-170.

85. Miettinen M, Lindenmayer AE, & Chaubal A (1994) Endothelial cell markers CD31, CD34, and BNH9 antibody to H- and Y-antigens--evaluation of their specificity and sensitivity in the diagnosis of vascular tumors and comparison with von Willebrand factor. *Mod Pathol* 7(1):82-90.

86. Lamszus K*, et al.* (2000) Vascular endothelial growth factor, hepatocyte growth factor/scatter factor, basic fibroblast growth factor, and placenta growth factor in human meningiomas and their relation to angiogenesis and malignancy. *Neurosurgery* 46(4):938-947; discussion 947-938.

87. Aguiar PH, Tsanaclis AM, Tella OI, Jr., & Plese JP (2003) Proliferation rate of intracranial meningiomas as defined by the monoclonal antibody MIB-1: Correlation with peritumoural oedema and other clinicoradiological and histological characteristics. *Neurosurg Rev* 26(3):221-228.

88. Amatya VJ*, et al.* (2001) Immunohistochemical study of Ki-67 (MIB-1), p53 protein, p21WAF1, and p27KIP1 expression in benign, atypical, and anaplastic meningiomas. *Hum Pathol* 32(9):970-975.

89. Kasuya H*, et al.* (2006) Clinical and radiological features related to the growth potential of meningioma. *Neurosurg Rev* 29(4):293-296; discussion 296-297.

90. Kim YJ, Ketter R, Steudel WI, & Feiden W (2007) Prognostic significance of the mitotic index using the mitosis marker anti-phosphohistone H3 in meningiomas. *Am J Clin Pathol* 128(1):118-125.

91. Kumar S*, et al.* (2014) Evaluation of 1p and 14q status, MIB-1 labeling index and progesterone receptor immunoexpression in meningiomas: Adjuncts to histopathological grading and predictors of aggressive behavior. *Neurol India* 62(4):376-382.

92. Nakaguchi H*, et al.* (1999) Postoperative residual tumor growth of meningioma

can be predicted by MIB-1 immunohistochemistry. *Cancer* 85(10):2249-2254.

93. Nakasu S, Fukami T, Jito J, & Nozaki K (2009) Recurrence and regrowth of benign meningiomas. *Brain Tumor Pathol* 26(2):69-72.

94. Nakaya K*, et al.* (2009) Risk factors for regrowth of intracranial meningiomas after gamma knife radiosurgery: Importance of the histopathological grade and MIB-1 index. *Minim Invasive Neurosurg* 52(5-6):216-221.

95. Oya S, Kawai K, Nakatomi H, & Saito N (2012) Significance of Simpson grading system in modern meningioma surgery: Integration of the grade with MIB-1 labeling index as a key to predict the recurrence of WHO Grade I meningiomas. *J Neurosurg* 117(1):121-128.

96. Perry A, Stafford SL, Scheithauer BW, Suman VJ, & Lohse CM (1998) The prognostic significance of MIB-1, p53, and DNA flow cytometry in completely resected primary meningiomas. *Cancer* 82(11):2262-2269.

97. Vankalakunti M, Vasishta RK, Das Radotra B, & Khosla VK (2007) MIB-1 immunolabeling: A valuable marker in prediction of benign recurring meningiomas. *Neuropathology* 27(5):407-412.

98. Yamaguchi S*, et al.* (2014) Prognostic factors for survival in patients with high-grade meningioma and recurrence-risk stratification for application of radiotherapy. *PLoS One* 9(5):e97108.

99. Tyagi A, Chakrabarty A, & Franks A (2004) MIB1 proliferation index in meningiomas: Does it predict recurrence? A clinicopathological study. *Br J Neurosurg* 18(4):357-361.

100. Roser F, Samii M, Ostertag H, & Bellinzona M (2004) The Ki-67 proliferation antigen in meningiomas. Experience in 600 cases. *Acta Neurochir (Wien)* 146(1):37-44; discussion 44.

101. Karja V, Sandell PJ, Kauppinen T, & Alafuzoff I (2010) Does protein expression predict recurrence of benign World Health Organization grade I meningioma? *Hum Pathol* 41(2):199-207.

102. Gousias K, Schramm J, & Simon M (2016) The Simpson grading revisited: Aggressive surgery and its place in modern meningioma management. *J Neurosurg* 125(3):551-560.

103. Abramovich CM & Prayson RA (1999) Histopathologic features and MIB-1 labeling indices in recurrent and nonrecurrent meningiomas. *Arch Pathol Lab Med* 123(9):793-800.

104. Abry E, Thomassen IO, Salvesen OO, & Torp SH (2010) The significance of Ki-67/MIB-1 labeling index in human meningiomas: A literature study. *Pathol Res Pract* 206(12):810-815.

105. Christoforidis GA, *et al.* (2012) "Tumoral pseudoblush" identified within gliomas at high-spatial-resolution ultrahigh-field-strength gradient-echo MR imaging corresponds to microvascularity at stereotactic biopsy. *Radiology* 264(1):210-217.

106. Kimura H, *et al.* (2006) Perfusion imaging of meningioma by using continuous arterial spin-labeling: Comparison with dynamic susceptibility-weighted contrast-enhanced MR images and histopathologic features. *AJNR Am J Neuroradiol* 27(1):85-93.

107. Yan R, *et al.* (2016) Non-Gaussian diffusion MR imaging of glioma: Comparisons of multiple diffusion parameters and correlation with histologic grade and MIB-1 (Ki-67 labeling) index. *Neuroradiology* 58(2):121-132.

108. Bitzer M, *et al.* (1998) Angiogenesis and brain oedema in intracranial meningiomas: Influence of vascular endothelial growth factor. *Acta Neurochir (Wien)* 140(4):333-340.

109. Fatima Z, *et al.* (2013) Associations among q-space MRI, diffusion-weighted MRI and histopathological parameters in meningiomas. *Eur Radiol* 23(8):2258-2263.

110. Chen W, *et al.* (2015) Overexpression of vascular endothelial growth factor indicates poor outcomes of glioma: A systematic review and meta-analysis. *Int J Clin Exp Med* 8(6):8709-8719.

111. Jain RK (2005) Normalization of tumor vasculature: An emerging concept in antiangiogenic therapy. *Science* 307(5706):58-62.

112. Elia AE, Shih HA, & Loeffler JS (2007) Stereotactic radiation treatment for benign meningiomas. *Neurosurg Focus* 23(4):E5.

113. Minniti G, Amichetti M, & Enrici RM (2009) Radiotherapy and radiosurgery for benign skull base meningiomas. *Radiat Oncol* 4:42.

114. Kaur G, *et al.* (2014) Adjuvant radiotherapy for atypical and malignant meningiomas: A systematic review. *Neuro Oncol* 16(5):628-636.

115. Rao Gogineni V, *et al.* (2010) Radiation-inducible silencing of uPA and uPAR in vitro and in vivo in meningioma. *Int J Oncol* 36(4):809-816.

116. Kargiotis O, *et al.* (2008) uPA/uPAR downregulation inhibits radiation-induced migration, invasion and angiogenesis in IOMM-Lee meningioma cells and decreases tumor growth in vivo. *Int J Oncol* 33(5):937-947.

117. Gogineni VR, *et al.* (2011) Chk2-mediated G2/M cell cycle arrest maintains radiation resistance in malignant meningioma cells. *Cancer Lett* 313(1):64-75.

118. Gogineni VR, *et al.* (2011) alpha3beta1 integrin promotes radiation-induced migration of meningioma cells. *Int J Oncol* 38(6):1615-1624.

119. Gupta R, *et al.* (2011) uPAR/cathepsin B overexpression reverse angiogenesis by rescuing FAK phosphorylation in uPAR/cathepsin B down regulated meningioma. *PLoS One* 6(2):e17123.

120. Nalla AK, Gogineni VR, Gupta R, Dinh DH, & Rao JS (2011) Suppression of uPA and uPAR blocks radiation-induced MCP-1 mediated recruitment of endothelial cells in meningioma. *Cell Signal* 23(8):1299-1310.

121. Gupta R, *et al.* (2011) Oncogenic role of p53 is suppressed by si-RNA bicistronic construct of uPA, uPAR and cathepsin-B in meningiomas both in vitro and in vivo. *Int J Oncol* 38(4):973-983.

122. Al-Khalaf HH, *et al.* (2008) Expression of survivin and p16(INK4a)/Cdk6/pRB proteins and induction of apoptosis in response to radiation and cisplatin in meningioma cells. *Brain Res* 1188:25-34.

123. Al-Khalaf HH, *et al.* (2007) The p53/p21 DNA damage-signaling pathway is defective in most meningioma cells. *J Neurooncol* 83(1):9-15.

124. Aarhus M, Lund-Johansen M, & Knappskog PM (2011) Gene expression profiling of meningiomas: Current status after a decade of microarray-based transcriptomic studies. *Acta Neurochir (Wien)* 153(3):447-456.

125. Moeller BJ & Dewhirst MW (2006) HIF-1 and tumour radiosensitivity. *Br J Cancer* 95(1):1-5.

126. Moeller BJ, Cao Y, Li CY, & Dewhirst MW (2004) Radiation activates HIF-1 to regulate vascular radiosensitivity in tumors: Role of reoxygenation, free radicals, and stress granules. *Cancer Cell* 5(5):429-441.

127. Guo K, *et al.* (2001) Hypoxia induces the expression of the pro-apoptotic gene BNIP3. *Cell Death Differ* 8(4):367-376.

128. An WG, *et al.* (1998) Stabilization of wild-type p53 by hypoxia-inducible factor 1alpha. *Nature* 392(6674):405-408.

129. Moeller BJ, *et al.* (2005) Pleiotropic effects of HIF-1 blockade on tumor radiosensitivity. *Cancer Cell* 8(2):99-110.